

Review

2D and Quasi-2D Halide Perovskite-Based Resistive Switching Memory Systems

Hyojung Kim ¹, Daijoon Hyun ¹, Muhammad Hilal ¹, Zhicheng Cai ¹ and Cheon Woo Moon ^{2,*}

¹ Department of Semiconductor Systems Engineering, Sejong University, 209, Neungdong-ro, Gwangjin-gu, Seoul 05006, Republic of Korea; hyojungkim0912@sejong.ac.kr (H.K.); djhyun@sejong.ac.kr (D.H.); hilal1991@sejong.ac.kr (M.H.); cai1121@sejong.ac.kr (Z.C.)

² Department of Display Materials Engineering, Soonchunhyang University, Asan 31538, Republic of Korea

* Correspondence: cwmoon@sch.ac.kr

Abstract: Resistive switching (RS) memory devices are gaining recognition as data storage devices due to the significant interest in their switching material, Halide perovskite (HP). The electrical characteristics include hysteresis in its current–voltage (I – V) relationship. It can be attributed to the production and migration of defects. This property allows HPs to be used as RS materials in memory devices. However, 3D HPs are vulnerable to moisture and the surrounding environment, making their devices more susceptible to deterioration. The potential of two-dimensional (2D)/quasi-2D HPs for optoelectronic applications has been recognized, making them a viable alternative to address current restrictions. Two-dimensional/quasi-2D HPs are created by including extended organic cations into the ABX_3 frameworks. By adjusting the number of HP layers, it is possible to control the optoelectronic properties to achieve specific features for certain applications. This article presents an overview of 2D/quasi-2D HPs, including their structures, binding energies, and charge transport, compared to 3D HPs. Next, we discuss the operational principles, RS modes (bipolar and unipolar switching), in RS memory devices. Finally, there have been notable and recent breakthroughs in developing RS memory systems using 2D/quasi-2D HPs.

Keywords: resistive switching memory; 2D halide perovskites; quasi-2D halide perovskites; 3D halide perovskites



Citation: Kim, H.; Hyun, D.; Hilal, M.; Cai, Z.; Moon, C.W. 2D and Quasi-2D Halide Perovskite-Based Resistive Switching Memory Systems. *Electronics* **2024**, *13*, 3572. <https://doi.org/10.3390/electronics13173572>

Academic Editor: Elias Stathatos

Received: 2 August 2024

Revised: 1 September 2024

Accepted: 6 September 2024

Published: 8 September 2024



Copyright: © 2024 by the authors. Licensee MDPI, Basel, Switzerland. This article is an open access article distributed under the terms and conditions of the Creative Commons Attribution (CC BY) license (<https://creativecommons.org/licenses/by/4.0/>).

1. Introduction

There has been significant interest in renewable energy devices due to a growing understanding of environmental and economic concerns. Renewable energy devices have been extensively researched as potential energy sources [1–3]. A typical semiconductor is a crystalline sheet that can efficiently collect and transfer charges over long distances. This property enables the use of silicon-based solar cells. Furthermore, researchers are examining highly potential photovoltaic technologies [4–6]. In this area, halide perovskites (HPs) have drawn attention as advanced materials within photovoltaics. The “perovskite” was identified in the Ural Mountains [7]. HPs have garnered significant scientific attention for their exceptional electrical properties and their cost-effective production and ability to be processed using solutions. “Perovskite” describes a crystal structure with the general formula ABX_3 [7–10].

The structure of HP consists of cations A and B, with A being bigger than B and an anion represented by X. The A, B, and X elements have specific, unchanging locations [7,8,11]. The three-dimensional (3D) structure of ABX_3 perovskites consists of an octahedral network that shares corners. More precisely, B cations are encompassed by X anions to create BX_6 [7,12]. HPs with the unit formula ABX_3 have been widely utilized in photovoltaics due to their advantageous electrical properties. These properties include an exceptionally long electron diffusion length, excellent charge carrier mobility, a broad absorption range,

and a high absorption coefficient [13,14]. In addition to their application in photovoltaics, HP materials possess remarkable electrical qualities that make them suitable for various next-generation devices [15–19]. HPs are expected to be the primary research subject for numerous applications in coming years. Hence, it is necessary to comprehend the structural and electrical characteristics of HPs thoroughly.

Nevertheless, 3D HPs are susceptible to moisture and the surrounding environment, making their devices more prone to degradation. The two-dimensional (2D) and quasi-2D HPs are identified as promising materials with great potential for optoelectronic applications, making them a solution to overcome existing limitations [7,20]. The 2D/quasi-2D HPs are created by incorporating elongated organic cations. They are too large to fit into the ABX_3 [21]. This review introduces the characteristics of quasi-2D HPs, for example structures, photoluminescence, binding energies, and charge transports compared to 3D HPs. The operating principles, resistive switching (RS) modes (bipolar and unipolar switching), and the switching mechanisms of RS memory devices are mentioned. Finally, 2D/quasi-2D HP-based RS memory devices are categorized with 2D single crystals, 2D/3D heterojunctions, 2D/quasi-2D, and lead-free 2D HPs.

2. HPs

2.1. Structures

Figure 1a demonstrates that ABX_3 perovskites possess 3D structures [7,22]. The cations and anions found at the A, B, and X sites are given in Figure 1b [7]. However, only the 742 kinds can occur within the tolerance range factor of 0.8–1. The Goldschmidt tolerance and octahedral factors can be employed to determine the geometric structures of precisely fitting 3D perovskites. The tolerance factor (t) is calculated with the ionic radii of A and X. The octahedral factor is calculated as the ratio of the ionic radius of B to the ionic radius of X. Figure 1c illustrates the tolerance factors [7]. The plot is based on the A cations, and the open symbols mean a nonperovskite structure. In order to obtain cubic perovskites, the t value should be within 0.8–1.0. Orthorhombic perovskite structures are obtained when the tolerance factor value is smaller than 0.8, while hexagonal noncubic perovskite structures are obtained when the tolerance factor value exceeds 1. Furthermore, the cubic perovskite structure requires that the octahedral factor be between 0.44 and 0.90 [22].

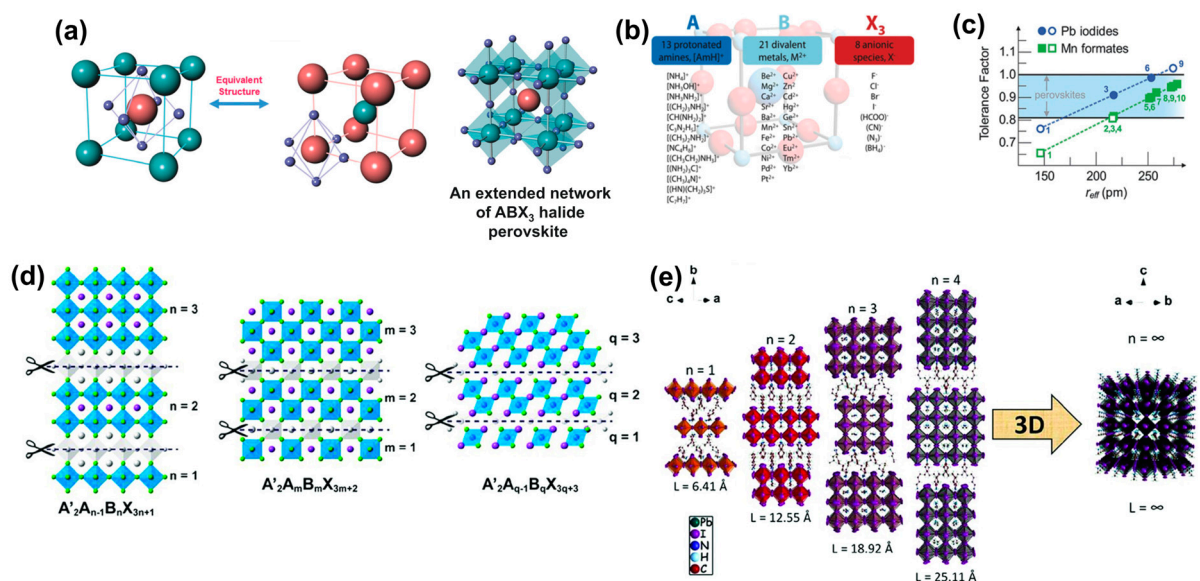


Figure 1. (a) General crystal structure of ABX_3 HP (pink spheres: A cations, green spheres: B cations, and purple spheres: X (halide) anions). (b) A, B, and X sites are listed. (c) Tolerance factors. Reproduced with permission [7]. Copyright 2018, Wiley-VCH. (d) Schematic of 2D/quasi-2D HPs. (e) Crystal structure of 2D, quasi-2D, and 3D HPs. Reproduced with permission [20]. Copyright 2019, Wiley-VCH.

Two-dimensional HPs comprise several atomic thin layers of HPs. Morphological 2D/quasi-2D HPs often arise via dimensional confinement during the crystallization of ABX_3 HPs [20]. This confinement occurs due to the growth process guided by long-chain organic ligands or the perovskites while maintaining their ABX_3 chemical formula. As an illustration, Tyagi et al. effectively produced $MAPbBr_3$ (MA: methylammonium) nanoplates with a thickness of a single unit cell by employing the colloidal synthesis method, utilizing long-chain organic ligands [23]. Ha et al. successfully produced 2D/quasi-2D HPs of excellent quality [24]. Using chemical vapor deposition techniques, they could control the thickness of these perovskites, which ranged from 10 to 140 nm. In contrast to structurally thin formations, the crystallographic 2D/quasi-2D HPs are created by cutting 3D HPs along the (100), (110), and (111) crystal orientation planes. This uses large organic spacers to produce three distinct families of layered HPs, as depicted in Figure 1d [20]. The chemical formulas for the (100), (110), and (111) orientated HP families are $A'_2A_{n-1}B_nX_{3n+1}$, $A'_2A_mB_mX_{3m+2}$, and $A'_2A_{q-1}B_qX_{3q+3}$, respectively. The (100) oriented layered HPs are extensively studied because of their exceptional resistance to various organic and inorganic components. The Ruddlesden–Popper (RP) HPs were derived from the resemblance of their crystal structure to inorganic RP perovskites [25]. The RP HPs are typically produced by dividing the 3D structure into varying thicknesses along the (100) direction [26]. The RP HPs consist of metal-halide octahedron slabs arranged in layers, with a bilayer of large organic cations sandwiched in between (Figure 1e) [20]. The majority of RP HPs consist of single amines as their organic molecules (R).

Hence, the revised expression for 2D RP can be $(RNH_3)_2MX_4$ or $(NH_3RNH_3)MX_4$, where M represents a metal cation. In the case of pure 2D HPs, each layer of PbX_6 octahedra is precisely positioned between two voluminous organic layers [7,27]. In order to enhance the layer count in RP HPs, it is necessary to introduce methylammonium (MA), formamidinium (FA), or inorganic cations such as cesium (Cs^+) into the structures of the HPs, in addition to the long-chain organic cations [28]. These combinations produce quasi-2D HPs with different formulas. It is important that an organic cation is necessary to develop interconnected multiple layers of corner-sharing MX_6 octahedra in quasi-2D HPs [29]. The variable n in these equations represents the number of 2D/quasi-2D HP layers. Specifically, when n equals 1, the HPs have a 2D structure, while quasi-2D HPs are formed for n values greater than or equal to 2. The inherent insulating nature of the bulky organic layers allows for the formation of numerous quantum well structures when combined with MX_6 octahedron layers [30].

2.2. Photoluminescence (PL)

Compared to 3D HPs, 2D/quasi-2D HPs exhibit a difference in absorption and PL known as the Stokes shift. Singldinger et al. examined HP nanoplatelets with two distinct thicknesses, namely two and three monolayers [31]. To evaluate the quality of the two separate dispersions, UV-vis and PL spectra were obtained (Figure 2a), which show distinct excitonic absorption peaks and single, tightly focused PL peaks at 435 for the two-monolayer and 457 nm for the three-monolayer nanoplatelets. The narrow PL peaks show complete widths at half-maximum of 76 and 104 meV, and tiny Stokes shifts of 60 and 61 meV. Transmission electron microscopy (TEM) presents additional support for this claim, as exemplified in Figure 2b,c for the two-monolayer nanoplatelets. The two-monolayer nanoplatelets have a square shape with a thickness of 1.3 ± 0.2 nm. The three-monolayer nanoplatelets have a quadratic shape, with a thickness of 1.9 ± 0.2 nm. The layout and proximity facilitate energy transfer mechanisms that rely on dipole–dipole interaction.

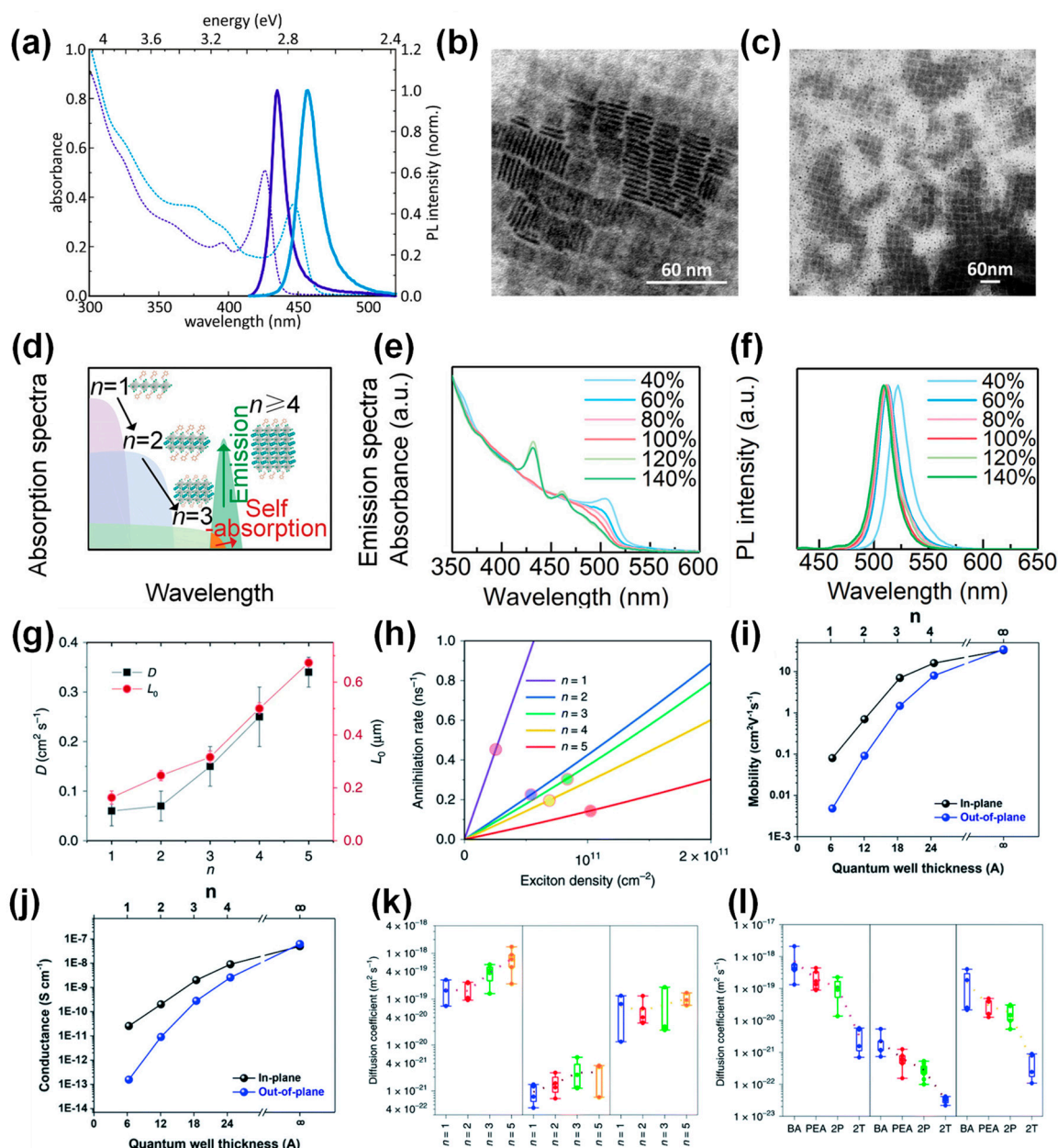


Figure 2. (a) Absorption and PL spectra (dashed lines and solid lines, respectively) of two- (purple) and three- (blue) monolayer nanoplatelets. (b) TEM images of two-monolayer nanoplatelets (thickness of 1.3 ± 0.2 nm). (c) TEM images of three-monolayer nanoplatelets (thickness of 19 ± 1 nm). Reproduced with permission [31]. Copyright 2020, American Chemical Society. (d) Energy transfer contributes to a more significant Stokes shift. (e) The absorption spectra of CsPbBr₃ with varying PEA content. (f) The photoluminescence spectra of CsPbBr₃. Reproduced with permission [32]. Copyright 2023, Wiley-VCH. (g) Carrier diffusion constant in 2D perovskites. (h) Annihilation rate in 2D perovskites. Reproduced with permission [33]. Copyright 2020, Springer Nature. (i) Carrier mobility in 2D perovskites. (j) Conductance in 2D perovskites. Reproduced with permission [34]. Copyright 2018, American Chemical Society (k) Comparison of the impact of the n value on the diffusion coefficients. (l) Comparison of the impact of the ligands on the diffusion coefficients. Reproduced with permission [35]. Copyright 2021, Springer Nature.

The Stokes shift is influenced by the thickness of crystallographic stacking layers. Liu et al. demonstrated quasi-2D perovskite materials utilizing a solution-based technique [32]. $C_6H_5CH_2CH_2NH_3^+(PEA^+)Cs_{n-1}Pb_nBr_{3n+1}$ was synthesized by introducing the

phenylethylamine cation (PEA⁺), a large organic cation, as Figure 2d depicts. The quasi-2D perovskites would lead to significant Stokes shifts through energy exchange across layers with varying n values. Figure 2e demonstrates that when the proportion of PEABr increases, the absorption peaks progressively intensify. This suggests the formation of phases with lower n values. The lack of an $n = 1$ absorption peak (403 nm) could be attributed to insufficient presence of this constituent. Simultaneously, due to the variation in phase distribution characterized by distinct n , the absorption band edge exhibited a progressive tilt. Figure 2f displays the emission spectra with varying PEABr content. The modest blue shift of the emission peak was ascribed to the dielectric confinement effect resulting from the presence of low n -value components in the surrounding distribution. In the case of quasi-2D perovskite with a PEABr concentration of 140%, the presence of an additional emission peak at 464 nm ($n = 3$) alongside the main emission peak at 508 nm is explained by incomplete energy transfer due to an excess of PEABr. Due to the slanted absorption band edge, the overlap between the emission and absorption spectra diminished as the PEABr increased.

2.3. Binding Energies

Most recent studies indicate that the exciton binding energy experiences a significant rise when the dimension of heterostructures is reduced from 3D to quasi-2D and 2D [36,37]. When a substance such as a semiconductor absorbs a photon, it generates an exciton, and the electrons and holes are drawn towards each other due to Coulomb interactions. Excitons can be classified into two categories: Wannier–Mott excitons, also known as free excitons, and Frenkel excitons, called tightly bound excitons [38,39]. Wannier–Mott excitons exhibit a high dielectric constant, which reduces the Coulomb interaction between electrons and holes owing to electric field screening [39]. As a result, the exciton binding energy is comparatively low.

Conversely, Frenkel excitons exhibit localized states strongly attached to particular atoms or molecules. As a result, the exciton binding energy is high, ranging from around 100 meV to 300 meV [27,36]. The excitons are required to cross the crystal by hopping energy transfer from one atom to another. Due to organic barriers, the excitons in 2D perovskites are restricted to the inorganic sheets. Due to their extremely thin nature, the inorganic sheets experience quantum confinement, significantly amplifying the Coulomb interactions. This effect is particularly pronounced in molecules of this type. Furthermore, the barrier rarely shields the Coulomb interactions within the wells because of the significant difference in the dielectric constants. As a result, the interaction between an electron and a hole becomes stronger, leading to significantly high binding energies of several hundreds of meV. Quasi-2D perovskites, such as those with $n = 40, 50, 60$, etc., exhibit smaller binding energies comparable to those of 3D perovskites [36]. However, the exciton binding energy is significant for small n values (i.e., $n < 5$) [40].

2.4. Charge Transports

When considering the 2D/quasi-2D HPs, it is crucial to evaluate and optimize the charge-carrier mobility, as these parameters play a significant role. Significantly, the mobilities of charge carriers or the lengths over which charge carriers diffuse in 2D/quasi-2D materials are significantly diminished compared to those of 3D HPs. Quasi-2D perovskites, with their tunable band structures and strongly bound excitons, are very suitable for optoelectronic applications, as they facilitate essential processes such as exciton transport and annihilation. Deng et al. utilized transient absorption microscopy to measure the dependence of exciton diffusion and annihilation on the value of n in perovskites [33]. This study revealed the significant influence of electron–hole interaction on this process. The exciton diffusion constant for $\text{BA}_2\text{MA}_{n-1}\text{Pb}_n\text{I}_{3n+1}$ grows as the thickness of the quantum well goes up. It ranges from 0.06 to 0.34 $\text{cm}^2 \text{s}^{-1}$ (Figure 2g). As n increases, the exciton annihilation decreases (Figure 2h). The distinctive characteristics of 2D perovskites are emphasized by their ability to transport excitons over long distances and their slow annihilation rate.

The electronic characteristics of quasi-2D HPs exhibit anisotropy due to their layered structure. Wang et al. conducted a study on the charge transport properties of $\text{BA}_2\text{MA}_{n-1}\text{Pb}_n\text{I}_{3n+1}$ [34]. In contrast, the out-of-plane properties were investigated using vapor plating. Due to van der Waals interactions in the out-of-plane direction, the carrier mobility and electrical conductivity consistently exceeded those in the out-of-plane direction (Figure 2i,j).

Nevertheless, the differences in these characteristics in the two directions diminish as the value of n grows, suggesting a decrease in anisotropy. The ion mobility inside the soft lattice of 2D HPs is influenced by the movement of charge carriers and the value of n . For example, Akriti et al. studied the impact of n and ligands on anionic diffusion by creating vertical heterostructures using various 2D HPs [35]. The vertical heterostructures consist of an upper layer of iodide perovskite and a lower layer of bromide perovskite. The anionic diffusion coefficient gradually increases by changing the value of n in the top $\text{BA}_2\text{MA}_{n-1}\text{Pb}_n\text{I}_{3n+1}$. This observation is consistent with three distinct diffusion models, indicating that halide migration is faster in perovskites with higher values of n (Figure 2k). The study found that larger p-conjugated ligands are successful in inhibiting the diffusion of halides compared to short-chain aliphatic ligands. This suggests that manipulating the structure or dimensions of molecules prevents the diffusion of anions (Figure 2l).

3. RS Memory Devices

3.1. The Operating Principles

The RS memory device has attracted considerable interest in nonvolatile memories because of its uncomplicated sandwich structure, fast operating speed, low power consumption, ability to store data at high densities, and scalability [22,41]. RS memory devices are deemed a favorable option for stretchy memory due to their simple structure and their benefits regarding data storage. The memory device was initially created following the identification of the TiO_2 -based RS device [42]. The RS memory device is a prevalent type of two-terminal device, specifically in oxide-based electronics, that consists of metal-insulator-metal components [43,44]. The memory elements comprise top and bottom electrodes with an insulating layer. In the metal-insulator-metal (MIM) stack, the uppermost electrode is subjected to an external bias and is exposed to either a voltage or a current. The upper electrodes mentioned above are formed by directly depositing metallic elements onto the RS layer. The bottom electrode is another electrode that serves as an electrically connected component.

By applying suitable voltage pulses to a device, it undergoes a transition from a state of high resistance (HRS) to a state of low resistance (LRS), which is widely known as “electroforming [45]”. Having devices bypassing the forming process is crucial to minimize the effects of high voltage stress during the initial operation. After the electroforming process, LRS transitions into an HRS when the RESET voltage is supplied oppositely. This alteration is widely recognized as the “RESET” procedure [22,46]. Subsequently, the shift from an HRS to an LRS takes place at the threshold voltage for the SET operation, which is different from the RESET procedure. To comprehend the RS operation, one must transition between the SET and RESET procedures. The transition from the SET to the RESET state signifies the “ON”, whereas the reverse behavior indicates the “OFF”. To minimize the risk of breakages in RS devices during the SET process, it is customary to limit the current level, known as current compliance (CC) [47].

To ensure the reliability of the RS device, it is crucial to have a substantial memory window, as well as durability and retention. Endurance quantifies the cycles required for reliable transition between the ON and OFF states [22,48]. Consequently, a higher endurance value indicates a more significant ability to handle programming tasks. Retention is a critical factor in nonvolatile memory technology, as it determines the duration the stored data are accessible before becoming inaccessible [22]. DRAM has a finite capacity to store data, so it needs to be refreshed often. The refresh processes lead to the inefficient utilization of power. Hence, the duration of data retention is intricately linked to energy

efficiency, a crucial factor given the escalating volume of data. Moreover, the ON/OFF ratio plays a crucial role in determining the memory window of a device. This significantly impacts the likelihood of operational errors occurring during the programming of the RS memory device. Hence, maximizing the ON/OFF ratio is necessary to guarantee reliable storage operation.

3.2. Bipolar and Unipolar RS Modes

The most common and extensively studied type of switching found in HP memory is bipolar RS. The memory device exhibits bipolar RS, which means it can only be activated by applying a forward bias and deactivated by applying a reverse bias. Figure 3a illustrates a hysteresis loop of current–voltage (I – V) during a sweep [49,50]. A sharp increase in current was seen when the swept voltage was from 0 V to around 1 V. A sudden increase in electrical current initiates the transition from the HRS to the LRS, progressing from state 1 to state 2. The OFF state can only be achieved when the film is returned to a voltage of 0 V. Following this, applying a negative bias results in a sudden increase in the resistance of the device when around -1.5 V is reached, causing the device to transition back to the HRS. This attribute is commonly observed in devices, facilitating easy transportation of carriers.

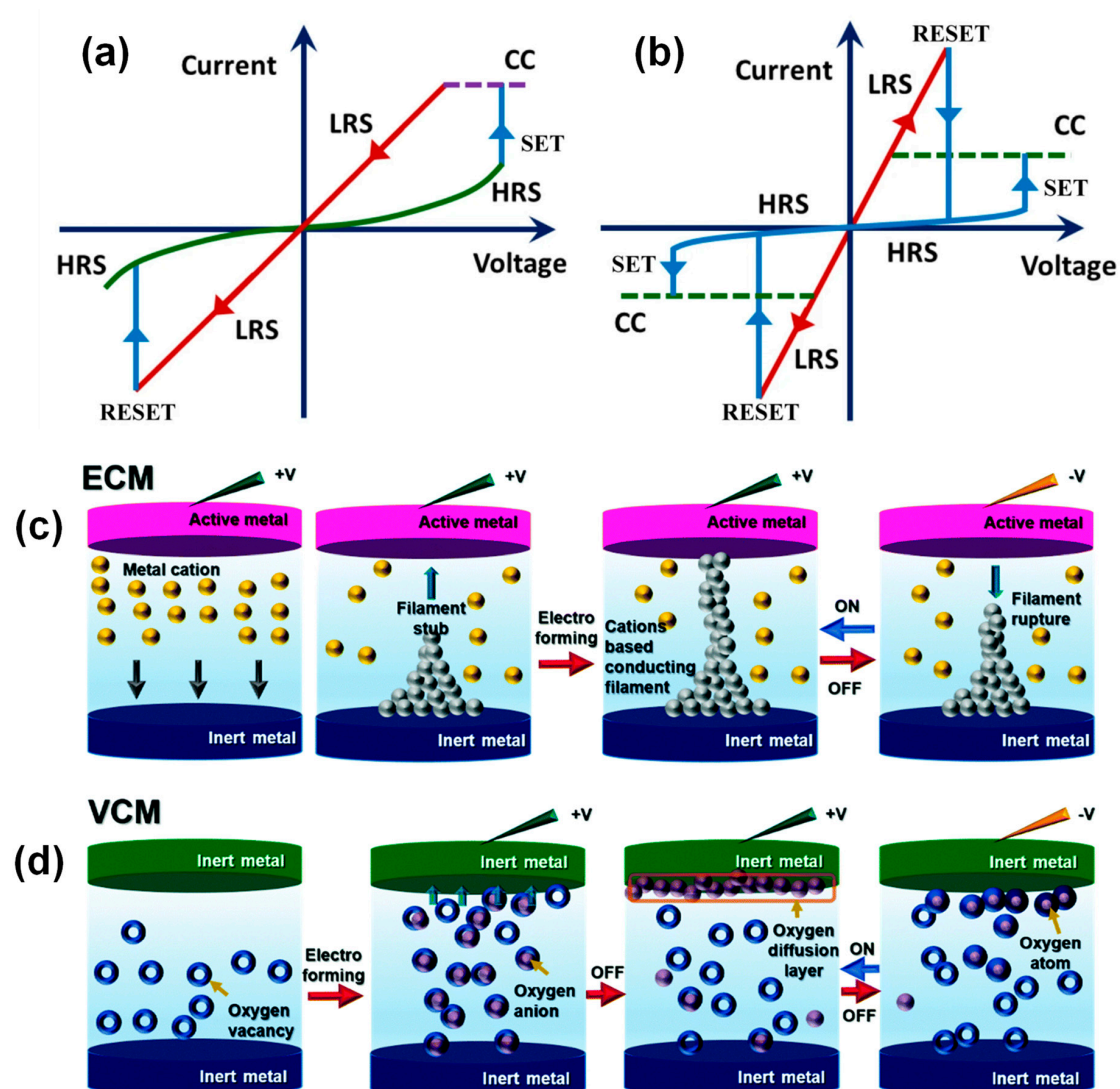


Figure 3. (a) I – V curves for bipolar switching mode. (b) I – V curves for unipolar switching mode. Reproduced with permission [49]. Copyright 2013, Springer. The RS mechanism; (c) ECM and (d) VCM. Reproduced with permission [22]. Copyright 2019, The Royal Society of Chemistry.

Although bipolar RS behaviors are more easily obtainable in HP-based devices, unipolar switching behavior is preferred due to its simplicity in allowing read–write activities. The development of unipolar RS in HP memory has rarely been studied. Unipolar switching uses the same biased direction in both the ON and OFF process. Figure 3b illustrates the characteristic of a unipolar RS behavior [49,50]. In contrast to bipolar RS, unipolar RS involves the ON and OFF process occurring within a similar direction of voltage. This process takes place under positive and negative voltage conditions. A minimal current flow characterizes the initial OFF state. The device turns on SET when the threshold voltage (V_{th}) reaches a high level. Generally, the V_{th} is more significant than bipolar RS. If the applied voltage exceeds the V_{th} , the device will be turned OFF. The same ON and OFF take place by reverse voltage. A high voltage bias can directly transform a pristine RS into an LRS. Therefore, the process is reversed.

3.3. The Operational Mechanisms of Resistive Switching Memory Devices

In recent years, extensive research has been conducted on the operational mechanisms of RS memory devices to predict and control their switching behaviors. This research aims to achieve optimal ON/OFF ratios, durability, retention, and sweep curves. This section presents two distinct operational processes of RS memory devices: the electrochemical mechanism (ECM) and the valence change mechanism (VCM).

The layers responsible for switching are usually dielectrics, and the essential aspects of RS depend on the migration of ions. The RS mechanism is dictated by the specific ion that undergoes migration within the dielectric material. The switching mechanisms of the ECM and VCM processes can be categorized as either filamentary or interface type [22,51]. VCM is a phenomenon seen in specific transition metal oxides, characterized by the movement of anions across the insulating layer [52]. The valence state is changed due to the redox process. Subsequently, there is a modification in the electronic conductivity of the insulating layer [53]. However, the ECM process shows a slight variation since it depends on the movement of cations from an electrode. Metal filaments are formed as cations are reduced, creating a conducting channel [48,54].

A recent study has discovered that the choice of the top electrode plays a vital role in defining the switching behavior of memory devices, in addition to other aspects. Generally, the top electrode is classified into two categories: active and inert metal [17,55,56]. Much research has been carried out to examine the influence of the top electrode on the RS characteristics of memory devices and its consequent impact on their overall performance. The electrochemical activity of the metals does not affect the functionality of the electrodes in VCM memory. However, electrochemical migration requires the movement of electrochemically active metal cations. Therefore, it is essential for one of the electrodes in an ECM memory device to possess a significant amount of electrochemical activity.

The ECM depends on electrochemical metallization, specifically on an active metal such as silver (Ag) or copper (Cu) [57–59]. The RS feature observed in ECM devices results from the creation and rupture of conducting filaments within the switching layer [60], also known as the insulating layer, as depicted in Figure 3c [22]. These procedures take place in the SET and RESET operations, respectively. The RS observed in the ECM process is primarily caused by the movement of metal cations from the active electrode [61]. When a positive voltage is provided, oxidation leads to the dissolution of the top electrode. Subsequently, the Ag cations migrate towards the platinum (Pt) bottom electrode due to the electric field [7,22,62]. The Ag cations are reduced through ion hopping and subsequently reach the Pt electrode. The spontaneous formation of a nucleus takes place when the concentration of Ag cations is above the supersaturation threshold, creating a filament that connects top and bottom electrodes [63,64].

However, Figure 3d depicts VCM-type memory devices [22]. Inert metals do not undergo any chemical reactions with the switching layer [65–67]. VCM refers to the process in which anion vacancies (defects) in the switching layer move in response to an electric field [48,68]. The migration is associated with modifying the valence of the cation

sublattice. The VCM mechanism plays a crucial role in comprehending the migration characteristics of oxide vacancies or ions [69,70]. The conventional approach to simulating valence-change RS memory involves the interplay of three interconnected phenomena: the creation of conductive filaments, the conduction mechanism, and the progressive increase in temperature. Redox reactions are essential for the creation and rupture of filaments in memory devices that use VCM [71]. The main factor responsible for RS in VCM is the migration of ions associated with defects inside the switching layer.

4. HPs-Based RS Memory Devices

HPs have been shown to exhibit ionic and electronic conduction activity in recent years. This unique characteristic makes them highly promising for RS memory devices, and they have attracted significant interest. Nevertheless, 3D perovskites face an issue: MA^+ plays a role in migration [48,72]. Devices are unable to achieve multilayer storage. And their issue is low moisture resistance. Two-dimensional HP materials possess a layered structure where organic and inorganic layers intertwine. This unique structure results in improved stability and reduced ion migration [20,48,73]. By including sizable organic cations in 2D perovskite structures, the detrimental effects of MA^+ migration on the resistance changes in 3D perovskite-based RS memory devices are avoided.

4.1. Two-Dimensional Single Crystal HP-Based RS Memory Devices

Di et al. investigated large-scale 2D $(PEA)_2PbI_4$ perovskite single crystals utilizing a modified space limitation approach [74]. Figure 4a depicts the orientation of 2D $(PEA)_2PbI_4$. The $(PEA)_2PbI_4$ consists of polyoctahedral sheets of PbI_4^{2-} arranged in a stack along the [001] direction. It indicates that most of the characteristic X-ray diffraction peaks of $(PEA)_2PbI_4$ perovskite will correspond to the {001} crystallographic plane. The inorganic layer of octahedron PbI_3^- is coupled using corner-sharing connectivity. The X-ray diffraction (XRD) patterns of the $(PEA)_2PbI_4$ single crystal are shown in Figure 4b, which shows no peaks corresponding to the reactants, indicating that the constructed 2D $(PEA)_2PbI_4$ has a high level of phase purity.

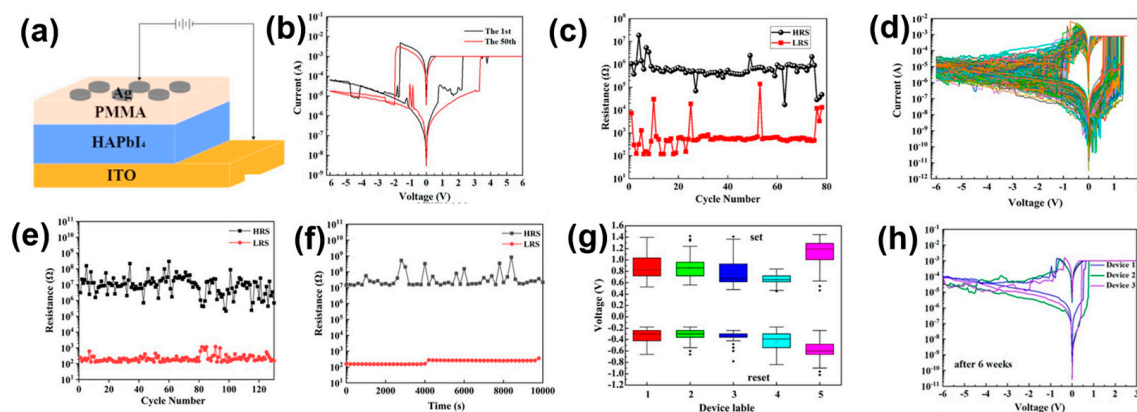


Figure 4. (a) The RS memory device structures of Ag/PMMA/HAPbI₄/ITO. (b) *I*–*V* curves of 50 switching cycles of Ag/HAPbI₄/ITO device. (c) Endurance data of Ag/HAPbI₄/ITO device. (d) *I*–*V* characteristics of 130 cycles of HAPbI₄-based device. (e) Endurance data of Ag/PMMA/HAPbI₄/ITO device. (f) Retention data of Ag/PMMA/HAPbI₄/ITO device. (g) Variation of *V*_{SET} and *V*_{RESET} for the five Ag/PMMA/HAPbI₄/ITO devices. (h) *I*–*V* curves of the three Ag/PMMA/HAPbI₄/ITO memory devices after 6 weeks. Reproduced with permission [75]. Copyright 2022, American Chemical Society.

As shown in Figure 4c, the *I*–*V* curves of the Au/ $(PEA)_2PbI_4$ /fluorine-doped tin oxide (FTO) device are measured when subjected to a voltage range from 0 V to 10 V and back to 0 V, followed by a sweep from 0 V to –10 V, and finally returning to 0 V. The voltage required to SET the device to the LRS is 4.2 V, and the ON/OFF ratio is approximately 10³. A

0 to -10 V voltage results in a comparable V_{RESET} of -4.2 V. Au/(PEA)₂PbI₄/FTO devices demonstrate a highly pronounced asymmetric bipolar RS phenomenon. In order to examine the potential influence of using Au and FTO electrodes on both ends of the device, the Au electrodes on both sides of the device are utilized to analyze whether the asymmetry of this bipolar RS phenomenon is attributed to the presence of asymmetric electrodes and its effect on the RS behaviors. Also, the I - V behavior of the Au/(PEA)₂PbI₄/Au device was measured when subjected to a voltage sweep of 0 V \rightarrow 10 V \rightarrow 0 V \rightarrow -10 V \rightarrow 0 V. The device, which consisted of Au/(PEA)₂PbI₄/Au with symmetrical electrodes, also displayed an asymmetric bipolar RS phenomenon, which is not influenced by the material of the electrodes.

Also, Liu et al. successfully synthesized a 2D C₅H₁₁N₃(HA)PbI₄ single crystal using a simple solution approach [75]. Figure 4a displays a schematic diagram of the Ag/Poly(methyl methacrylate) (PMMA)/HAPbI₄/indium tin oxide (ITO) device structure. The HAPbI₄ film serves as the functional layer, while a PMMA film is applied as a protective layer on top of the HAPbI₄ film. The Ag electrode is located at the top, while the ITO electrode is at the bottom. Figure 4b displays the I - V characteristics of the Ag/HAPbI₄/ITO device during the 1st and 50th switching cycles. Even after undergoing 50 cycles, the RS behavior is still present. Figure 4c displays the endurance of the device. The ON/OFF ratio of the memory decreased from 1000 to below 10. It might be attributed to a chemical interaction between the upper Ag electrode and HAPbI₄, resulting in the formation of AgI_x and a notable presence of iodine vacancies within HAPbI₄. Consequently, this leads to the degradation of the Ag electrode, which causes the equipment to experience rapid deterioration.

Figure 4d displays the I - V characteristics of the HAPbI₄-based device, revealing slight variations. These changes occur in defined increments and typically 400 steps every cycle. It should be noted that the HAPbI₄-based device exhibits consistent and reversible changes in resistance. The device exhibits a considerable ratio of high HRS to LRS, with a factor of almost 10^5 readings at 0.1 V. This ratio is sufficient to differentiate (Figure 4e). Furthermore, retention time was measured on the HRS and LRS. Figure 4f shows that there have been no notable alterations for a duration exceeding $10,000$ s. The HAPbI₄-based devices demonstrated reliable endurance and retention behaviors, confirming their data store capacity. The switching voltages between low and HRS were retrieved, as depicted in Figure 4g. It is essential to notice that the switching uniformity is reproducible. Following 6 weeks of exposure to ambient air, the RS characteristics of the HAPbI₄-based devices were reevaluated. The I - V characteristics of the three devices are depicted in Figure 4h. In addition, the retention times of the device were measured. The ON/OFF ratio was sufficiently large, surpassing 10^4 , and it remained constant at 8500 s. Compared to its value 6 weeks earlier, the resistance of the HRS has remained relatively stable, whereas the resistance of the LRS has increased by approximately 10.

4.2. Two-Dimensional/3D HPs Heterojunction-Based RS Memory Devices

Xia et al. utilized a 2D/3D heterostructure to fabricate RS memory devices [76]. In order to evaluate the impact of 2D perovskite, the I - V curves were measured. In Figure 5a, a direct current (DC) voltage sweep was applied, and the Al/MAPbI_{3-x}Cl_x(3D)/ITO device showed an ON/OFF ratio of less than 10. However, introducing BAI significantly enhanced Al/BAI(2D)/MAPbI_{3-x}Cl_x(3D)/ITO device performance. In Figure 5b, the resistance transitions from the HRS to the LRS at around 0.79 V. After applying a negative voltage, the current shows a sharp decrease at -0.77 V while changing from 0 to -1.3 V. Figure 5c shows that the RS characteristic continued for over 300 cycles. Furthermore, the current HRS and LRS values were observed at a readout voltage of 0.25 V in order to assess the cycling endurance of the device following BAI treatment. Figure 5d shows that the high ON/OFF ratio 10^3 remains stable without any notable variations even after 300 cycles. The HRS and LRS remain stable without noticeable variation during the $10,000$ s. The device continues to exhibit an effective ON/OFF ratio, as shown in Figure 5e. In order to confirm the reproducibility of the RS behavior, I - V curves were measured, as well as the current distribution in three randomly chosen devices, both in the LRS and the HRS.

Figure 5f demonstrates that the memory behaviors are identical, indicating a high constancy. Figure 5g,h illustrate the current distribution in the HRS and LRS of these devices. The current HRS and LRS are similar in all three devices, with no noticeable variation observed across the different devices. This demonstrates that the 2D/3D perovskite heterostructure has exceptional reliability and operational stability.

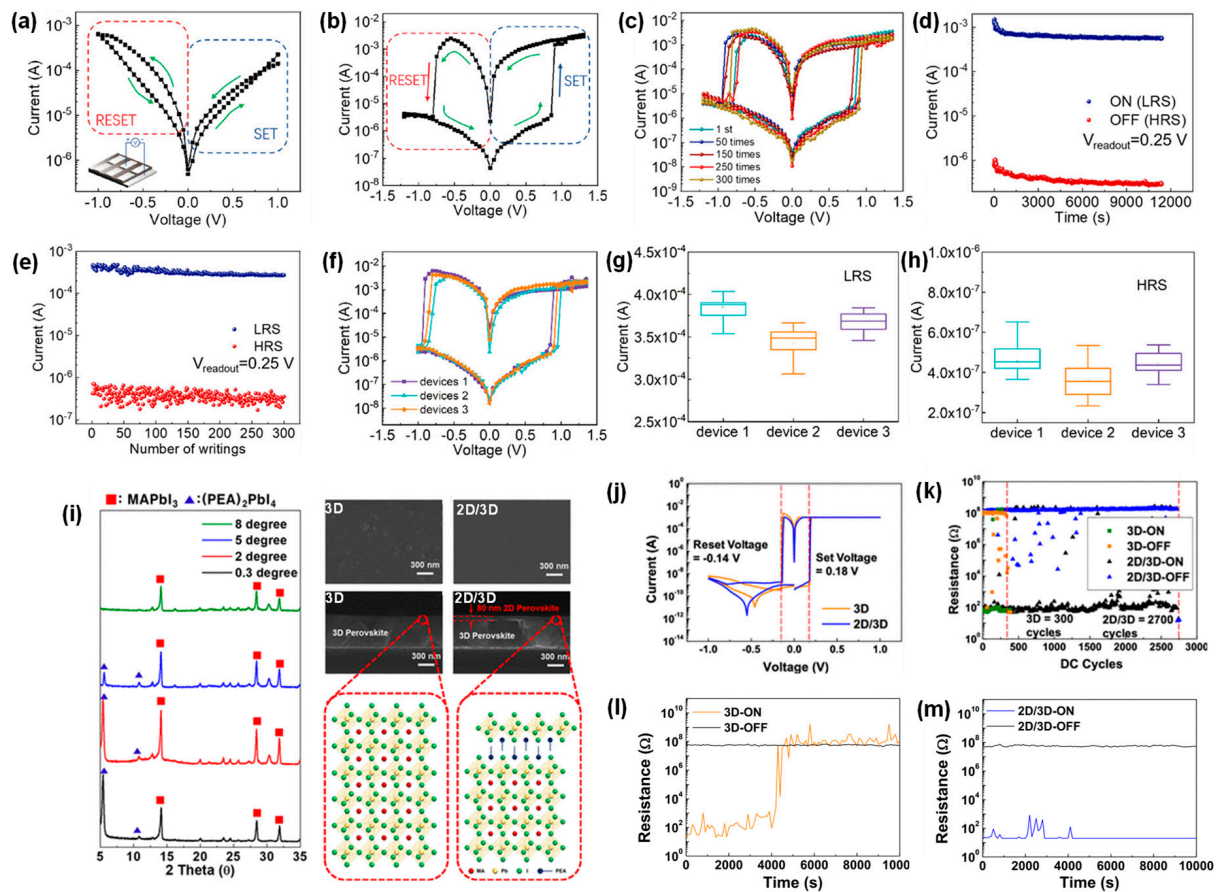


Figure 5. (a) I - V curves of $\text{MAPbI}_{3-x}\text{Cl}_x$ -based devices. (b) I - V curves of 2D/3D heterostructure memory devices. (c) I - V curves of 2D/3D memory devices at first and after 300 sweeping time measurements. (d) Retention data of 2D/3D heterostructure memory devices. (e) Endurance data of 2D/3D heterostructure memory devices. (f) I - V curves of three different devices. (g) The current distribution of the LRS for three different devices. (h) The current distribution of the HRS for three different devices. Reproduced with permission, [76]. Copyright 2020, American Chemical Society. (i) XRD patterns of the 2D/3D HP film (left). The plane view of SEM images and cross-sectional SEM images (right). (j) I - V characteristics of 2D and 2D/3D HP-based memory devices. (k) The endurance data of 2D and 2D/3D HP-based memory devices. (l) Retention time of 3D HP-based memory devices. (m) Retention time of 2D/3D HP-based memory devices. Reproduced with permission [77]. Copyright 2020, American Chemical Society.

Also, Lee et al. fabricated RS memory devices by using a low-temperature all-solution technique to build heterojunction structures of 2D perovskite (PEA_2PbI_4) and 3D perovskite (MAPbI_3) [77]. A layer of 2D perovskite was applied onto the 3D perovskite film using a spin-coating technique. Figure 5i shows XRD patterns at various angles of incidence. The primary peaks seen while employing MAPbI_3 as the 3D perovskite film are 14.12° , 28.46° , and 31.88° . These peaks correspond closely to the (110), (220), and (310) planes, respectively [78–80]. The peaks reported for PEA_2PbI_4 are located at 5.4° and 10.82° [81–83]. The XRD patterns showed that the PEA_2PbI_4 peak disappeared when the incidence angles exceeded 8° . In Figure 5i, the 3D perovskite layer has a thickness of 500 nm. Also, its

grain size is 100 nm. The 2D perovskite layer, around 80 nm thick, completely covers the 3D perovskite. The MAPbI₃ comprises the MA⁺ ion enclosed by PbI₆ octahedra. Therefore, the PEA₂PbI₄ layer is placed directly above the MAPbI₃ layer. Figure 5j displays the *I*–*V* behavior of the devices based on HP. The properties of the 2D/3D layer closely resemble those of the original 3D layer, displaying bipolar RS at approximately ±0.18 V. The devices preserved an HRS at approximately 10^{−10}. Subsequently, the existing levels were significantly increased to the LRS at approximately 10^{−3} A. Figure 5k displays the durability of a 2D/3D and 3D device. The 3D device shows 350 cycles. Nevertheless, the endurance test showed that the durability of the 2D/3D device was significantly increased, to approximately 2700 cycles. In Figure 5l, the 3D device demonstrated a retention time of up to 4100 s, whereas the 2D/3D device sustained over 10,000 s, in Figure 5m.

The 2D HP (pseudohalide-induced 2D MA₂PbI₂(SCN)₂) with pseudohalide (SCN[−]) substitution exhibited excellent resistance to moisture due to the more significant binding of SCN[−] ligands to Pb²⁺ compared to hydroxyl groups. Pan et al. fabricated RS memory devices based on 3D/2D HP by implementing PEASCN treatment [84]. The perovskite RS memory devices were fabricated using the Al/MAPbI_{3−x}Cl_x/2D/ITO structure (Figure 6a). Figure 6b,c display the consistency graphs of 1000 voltage scans for devices based on 3D and 3D/2D, respectively. The device featuring the 3D/2D perovskite exhibited exceptional uniformity throughout 1000 cycles of *I*–*V* curves. Furthermore, the endurance were measured at 0.2 V for the 3D and 3D/2D devices in Figure 6d,e. The 3D/2D device maintained a consistent window of 10³ with minimal variation throughout 1000 cycles. The resistance distribution is illustrated in Figure 6f,g. The 3D/2D device demonstrated a noticeably narrower range of resistance distribution than the 3D device. The resistance was measured using a 0.2 V_{read} to assess the dependability of the 3D/2D device, as shown in Figure 6h. Throughout the 10,000 s, the HRS and LRS remained consistently steady, keeping a constant window.

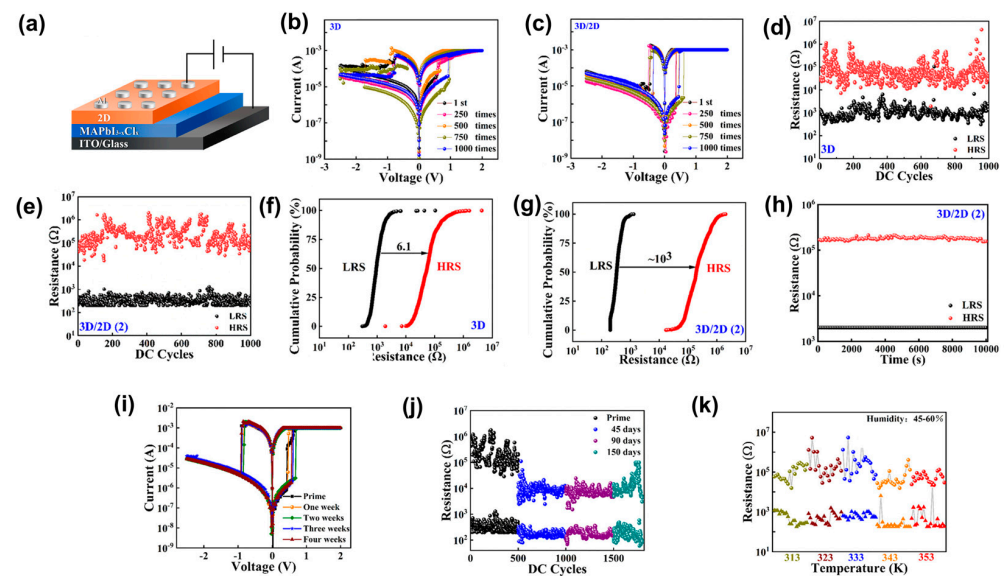


Figure 6. (a) Schematic illustration and 3D/2D perovskite device. (b) *I*–*V* curves in 1000 cycles of 3D devices. (c) *I*–*V* curves in 1000 cycles of 3D/2D perovskite devices. (d) Endurance cycles of 3D perovskite devices. (e) Endurance cycles of 3D/2D perovskite devices. (f) Statistical distribution of HRS and LRS of 3D perovskite devices. (g) Statistical distribution of HRS and LRS. (h) Retention time of 3D/2D perovskite devices over 10⁴ s. (i) *I*–*V* curves of 3D/2D perovskite devices. (j) Endurance data over 500 cycles for 150 days. (k) Endurance data of the 3D/2D perovskite device. Reproduced with permission [84]. Copyright 2023, American Chemical Society.

In order to assess the environmental durability with and without the 2D layer, the device was evaluated over 150 days in a low-humidity air environment. Figure 6i illustrates

the constancy of the device stored for various durations. The device exhibited exceptional durability over an extended period. Figure 6j demonstrates the endurance test after being stored in the air for 150 days. The device exhibited stability and an LRS transition that remained. To examine the durability of the devices in a challenging environment, the device stability was measured to ensure they withstand varied temperatures, in Figure 6k. The devices could function at temperatures as high as 353 K. Nevertheless, the device performance steadily deteriorated as the temperature rose above 353 K. The octahedral skeleton of PbX_6 structure can be disrupted by the volatilization of halogen ions caused by elevated temperatures [85]. The devices featuring 3D/2D perovskite exhibited exceptional long-term stability.

4.3. Two-Dimensional/Quasi-2D HPs-Based RS Memory Devices

Since the initial discovery of the first 2D $BA_2MA_{n-1}Pb_nI_{3n+1}$, other 2D HPs have been employed as functional layers in RS memory devices. Several methodologies have been employed to achieve high-performance RS memory devices, including perovskite composition engineering, interface engineering, and electrode tuning. This section will comprehensively discuss the current advancements in 2D and quasi-2D HPs-based RS memory devices.

Jeong et al. investigated an $Au/(RNH_3)_2(FA)_1Pb_2Br_7/ITO$ memory device using a binary oleylamine in Figure 7a [86]. Figure 7b shows the hysteresis behavior of the 3D $FAPbBr_3$ perovskite device. In Figure 7c, particularly, the $(RNH_3)_2(FA)_1Pb_2Br_7$ device is initially in the HRS, where the current progressively increases from 10^{-7} to 10^{-3} A when a voltage of 0 to 4 V is applied. Current from 10^{-3} to 10^{-1} A rises suddenly and significantly when a voltage threshold of 1.38 V is attained. The $(RNH_3)_2(FA)_1Pb_2Br_7$ compound retains during the subsequent positive reverse sweep and the next negative scan. In Figure 7d, the ON/OFF ratio progressively rose to 10^3 levels when the ligand concentration approached 1.2 vol%, and then towards saturation. And the ON/OFF ratio 10^3 was kept constant even at increased ligand concentrations. Figure 7e shows the relationship between thickness and ON/OFF ratios of the device. Up to 20 nm, the devices showed a rapid rise in the current ON/OFF ratio; after that, their current ON/OFF ratio increased gradually to 108 nm. And the ON/OFF ratio no longer grew but rather hit a saturation point as the thickness of the device increased.

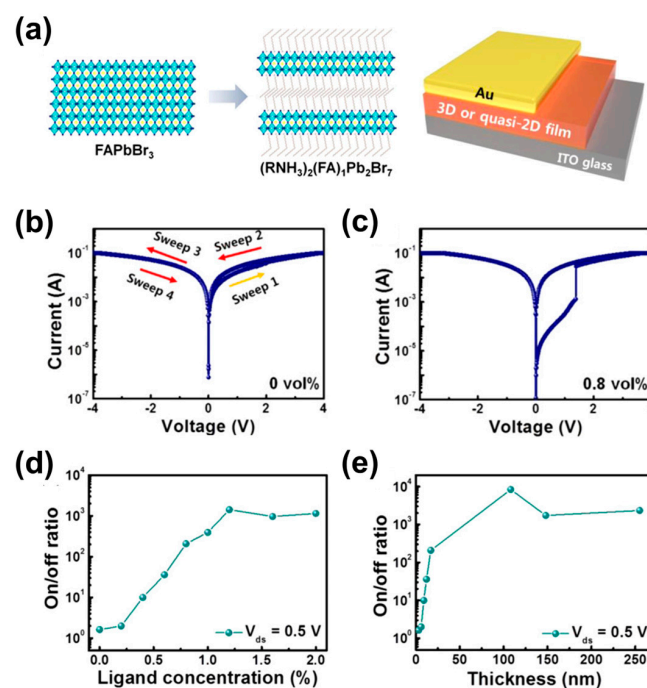


Figure 7. (a) Schematic of $FAPbBr_3$ and $(RNH_3)_2(FA)_1Pb_2Br_7$ structures and schematics of the device. (b) I - V curve of $FAPbBr_3$ -based memory device (0 vol%). (c) I - V curve of $(RNH_3)_2(FA)_1Pb_2Br_7$ -based

memory device with ligand concentrations of 0.8 vol%. (d) ON/OFF ratio according to the concentration. (e) ON/OFF ratio with various film thickness. Reproduced with permission [86]. Copyright 2021, American Chemical Society.

Also, Seo et al. conducted a study on the RS behaviors of $(\text{BA})_2(\text{MA})_{n-1}\text{Pb}_n\text{I}_{3n+1}$ compounds with different values of n (ranging from 1 to 3 and $n = \infty$) [87]. The study aimed to investigate how the structural transition from 3D (MAPbI_3) to 2D (BA_2PbI_4) HPs affects the RS behavior. Notably, 2D HPs were found to exhibit superior reliability and durability in switching, surpassing quasi-2D and 3D HPs. Figure 8a–d display the I – V characteristics obtained. The CC for the SET procedure was 10^{-2} A, whereas it was 10^{-1} A for the RESET process. It is observed that the SET voltage falls as the dimensionality transitions from 3D to 2D. Figure 8e illustrates the comparison of the SET voltage, represented by the electric field. The electric field was measured to be 0.47×10^6 , 0.52×10^6 , and 0.45×10^6 V m^{-1} for the MAPbI_3 , $\text{BA}_2\text{MA}_2\text{Pb}_3\text{I}_{10}$, and $\text{BA}_2\text{MAPb}_2\text{I}_7$, respectively. In contrast, the BA_2PbI_4 shows a considerably lower electric field of 0.25×10^6 V m^{-1} . The low electric field in BA_2PbI_4 suggests that the SET and RESET operations are more easily performed in 2D structures than in 3D or quasi-2D structures. Figure 8f presents a comparison of the ON/OFF ratio of BA_2PbI_4 and $\text{BA}_2\text{MAPb}_2\text{I}_7$, demonstrating a high ON/OFF ratio of approximately 10^7 . In contrast, the ON/OFF ratio decreases to around 10^5 in $\text{BA}_2\text{MA}_2\text{Pb}_3\text{I}_{10}$ and 10^2 in MAPbI_3 . Figure 8g displays the endurance properties of BA_2PbI_4 , $\text{BA}_2\text{MA}_1\text{Pb}_2\text{I}_7$, and $\text{BA}_2\text{MA}_2\text{Pb}_3\text{I}_{10}$. The pulse width was 10 ms, repeated for over 250 cycles. The Ag/ BA_2PbI_4 /Pt device demonstrates RS over 250 cycles. In contrast, quasi-2D perovskites exhibit increasingly unstable switching behavior, due to the instability of the HRS. The increased HRS stability for the 2D configuration, as compared to the quasi-2D configuration, suggests that residual filaments at the HRS occur less frequently in the 2D configuration than in the quasi-2D configuration [88]. In addition, the retention time is shown in Figure 8h. The SET retention demonstrates that 2D/quasi-2D HPs stay constant for 1000 s. The LRS resistance drops progressively from 50 Ω (BA_2PbI_4) to 33 Ω ($\text{BA}_2\text{MAPb}_2\text{I}_7$) and further to 27 Ω ($\text{BA}_2\text{MA}_2\text{Pb}_3\text{I}_{10}$). The conducting filament has a cylindrical shape; a decrease in resistance suggests that the radius of the conducting filament increases with the amount of MA. Consequently, as the radius of the filament rises, the amount of energy and time needed for it to break will also increase.

Also, Kim et al. used $\text{PEA}_2\text{Cs}_3\text{Pb}_4\text{I}_{13}$ and CsPbI_3 as RS elements [89]. Figure 9a illustrates the fabrication of a $(\text{PEA})_2\text{Cs}_3\text{Pb}_4\text{I}_{13}$ device with Ag top and Pt bottom electrodes. Figure 9b,c show the I – V curves of the CsPbI_3 and $(\text{PEA})_2\text{Cs}_3\text{Pb}_4\text{I}_{13}$ -based devices to assess the switching properties of the memory devices. The CC was 10^{-3} A for the SET process and 10^{-2} A for the RESET process. The ON/OFF ratio was approximately 10^9 , significantly higher than the ratio for the devices based on CsPbI_3 . The Schottky barrier height can account for the high ON/OFF ratio observed in devices based on $(\text{PEA})_2\text{Cs}_3\text{Pb}_4\text{I}_{13}$. The heightened barrier height decreased the density of injected carriers from the electrode to the perovskite switching layer. The energy barrier of quasi-2D perovskite restricts the movement of carriers from the Ag top electrode to the perovskite switching layer [90–92]. Thus, the current in the HRS is reduced, resulting in a high ON/OFF ratio. Figure 9d illustrates the Schottky barrier heights of the two perovskite materials. It suggests that the modification of the bandgap influences the barrier height by causing band bending [93,94]. Figure 9e displays the endurance properties of the $(\text{PEA})_2\text{Cs}_3\text{Pb}_4\text{I}_{13}$ memory device. These pulses had a duration of 640 μs , and a voltage of +0.05 V was applied during the read process. The Ag/ $(\text{PEA})_2\text{Cs}_3\text{Pb}_4\text{I}_{13}$ /Pt device demonstrated functionality for 230 endurance cycles, exhibiting ON/OFF ratios above 10^8 . In Figure 9f, the ON/OFF ratio remained constant at around 10^9 for almost 2000 s, while the reading voltage was SET at +0.02 V. A minor current fluctuation was detected in the HRS region. In contrast, the HRS and LRS remained consistently stable.

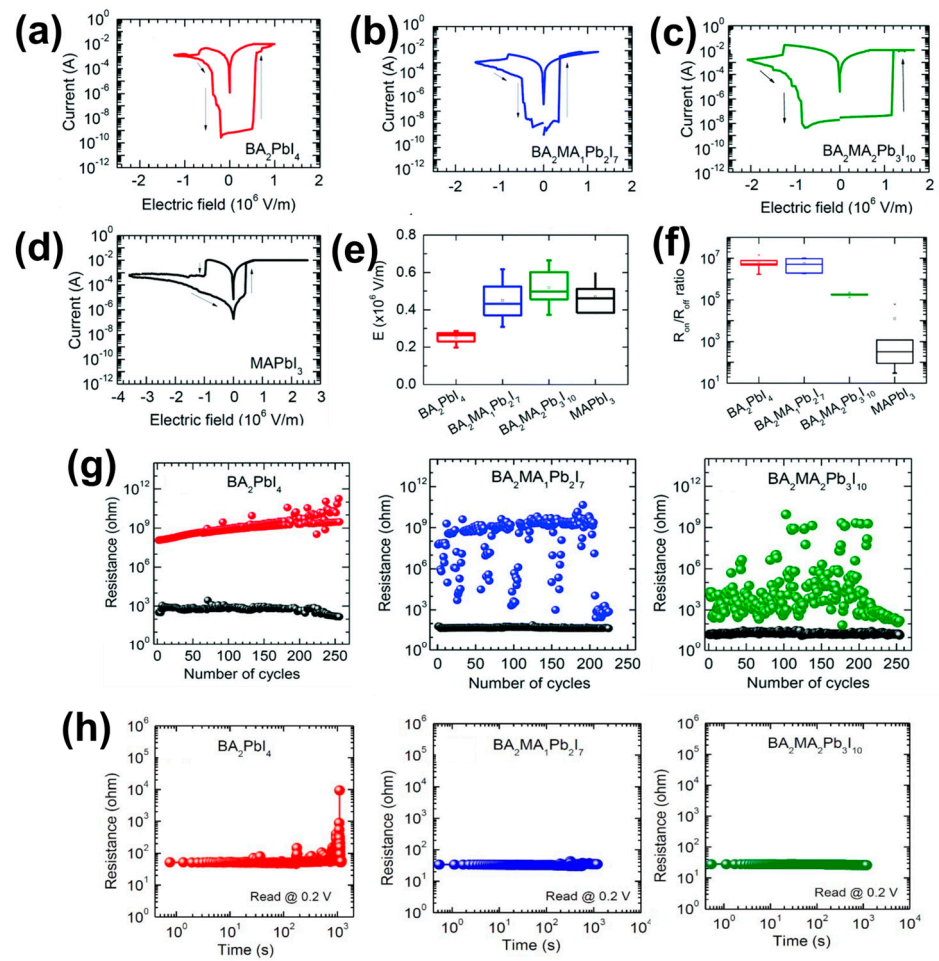


Figure 8. (a) *I*–*V* curves of BA₂PbI₄. (b) *I*–*V* curves of BA₂MAPb₂I₇. (c) *I*–*V* curves of BA₂MA₂Pb₃I₁₀. (d) *I*–*V* curves of MAPbI₃. (e) The operating voltage for the SET process. (f) The ON/OFF ratio for each material. (g) Endurance characteristics of BA₂PbI₄, BA₂MA₁Pb₂I₇, and BA₂MA₂Pb₃I₁₀-based memory devices. (h) Retention for LRS of BA₂PbI₄, BA₂MA₁Pb₂I₇, and BA₂MA₂Pb₃I₁₀-based memory devices. Reproduced with permission [87]. Copyright 2017, The Royal Society of Chemistry.

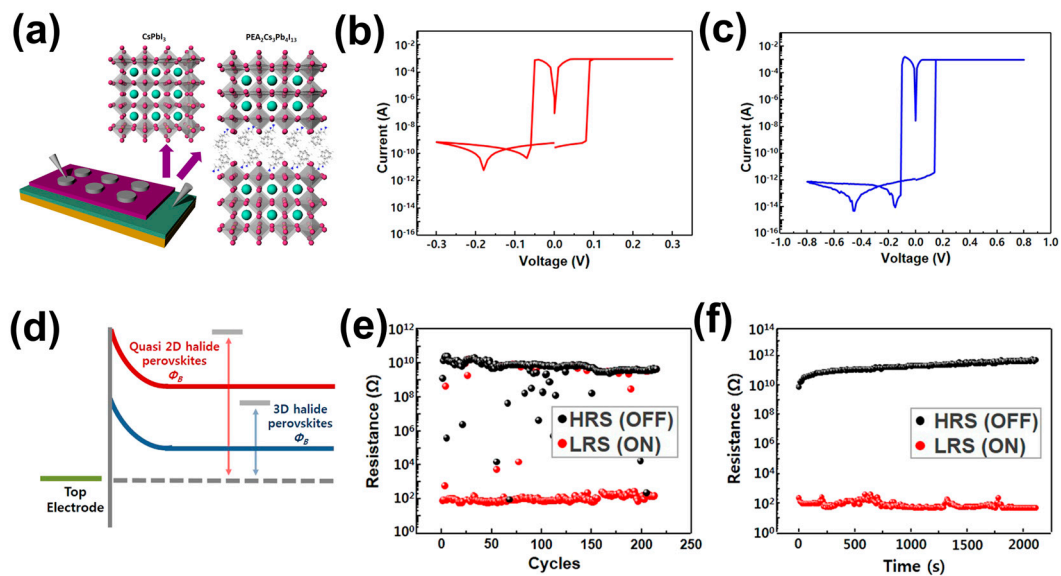


Figure 9. (a) The RS memory device structure and CsPbI₃ and (PEA)₂Cs₃Pb₄I₁₃. (b) *I*–*V* curves of Ag/CsPbI₃/Pt devices. (c) *I*–*V* curves of Ag/(PEA)₂Cs₃Pb₄I₁₃/Pt devices. (d) The Schottky barrier

heights for CsPbI_3 and $(\text{PEA})_2\text{Cs}_3\text{Pb}_4\text{I}_{13}$. (e) Endurance data for the $(\text{PEA})_2\text{Cs}_3\text{Pb}_4\text{I}_{13}$ memory device. (f) Retention property for the $(\text{PEA})_2\text{Cs}_3\text{Pb}_4\text{I}_{13}$ memory device. Reproduced with permission [89]. Copyright 2020, Springer Nature.

Kim et al. investigated $\text{PEA}_2\text{MA}_4\text{Pb}_5\text{I}_{16}$, which would be appropriate for a comparative analysis of vertical alignment degree [95]. Random and orientated $\text{PEA}_2\text{MA}_{n-1}\text{Pb}_n\text{I}_{3n+1}$ films formed without and with MAI additions, respectively. The 8×8 crossbar array devices are depicted in Figure 10a,b. Figure 10c depicts the electroforming process (dashed) and the SET and RESET process (solid). Applying electric bias fields, the orientated device displayed a low E-field in comparison to the random memory device. Enhanced charge transport behavior is indicated by the more significant current in the orientated device. Iodine vacancies have a low activation, so applying electric fields generates primarily formed filaments consisting of iodine vacancies. The vertically oriented perovskite is proposed to efficiently promote iodine vacancy migration along the vertical orientation, accelerating the electroforming E-field. Also, bipolar RS properties at a low electric field with an ON/OFF ratio above 10^2 were observed in both the random and directed devices. XRD patterns in Figure 10d are compared before and after the entire patterning process. Fifty I - E curves were examined in random (Figure 10e) and orientated (Figure 10f) devices. The statistical distributions (in Figure 10g,h) clearly illustrate that changes in the SET and RESET process and their LRS and HRS were more consistent in orientated devices than in random devices. I - E curves for the random (Figure 10i) and orientated (Figure 10j) crossbar arrays were assessed for device-to-device variability. Figure 10k,l show the associated statistical distribution. While the SET E-field and LRS showed only a minor improvement, the variations were much lower in the orientated device.

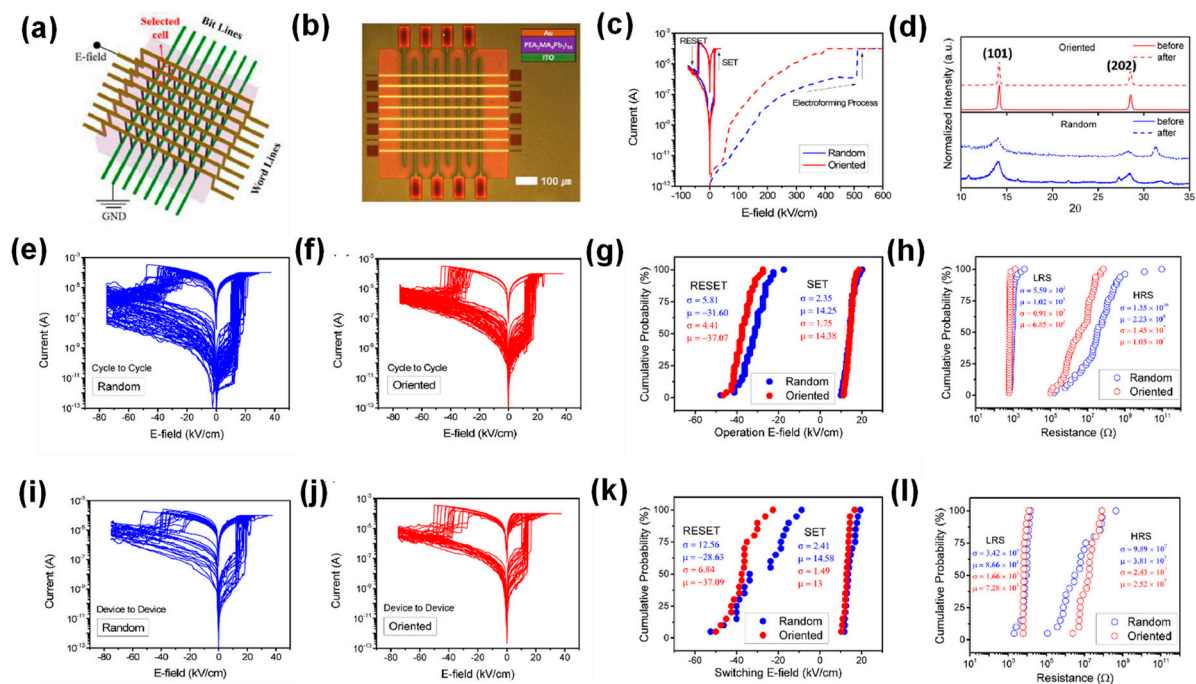


Figure 10. (a) A Schematic of the crossbar array. (b) The optical image of the crossbar array. (c) Switching properties with an ON/OFF ratio above 10^2 were observed in both the random and directed devices. (d) XRD patterns are compared before and after the entire patterning process. (e) Fifty I - E curves in random devices to estimated cycle-to-cycle variations. (f) Fifty I - E curves in orientated devices to estimated cycle-to-cycle variations. (g) The statistical distribution of E-field of cycle-to-cycle variations. (h) The statistical distribution of resistance of cycle-to-cycle variations. (i) I - E curves in random devices. (j) I - E curves in orientated devices to estimated device-to-device variations. (k) The statistical distribution of E-field of device-to-device variations. (l) The statistical distribution of resistance of device-to-device variations. Reproduced with permission [95]. Copyright 2022, Elsevier.

4.4. Lead-Free HP-Based RS Memory Devices

While the 2D HPs have demonstrated exceptional RS characteristics, the presence of lead in these materials remains a concern due to its toxicity. Regardless of the small quantity of lead, it could potentially harm the ecosystem. Consequently, many endeavors have been undertaken to explore lead-free HPs. In general, lead (II) can be substituted with non-toxic elements.

Kim et al. reported that 2D $(BzA)_2CuBr_4$ ($BzA = C_6H_5CH_2NH_3$) has anisotropic magnetic properties applied to RS memory devices [96]. The RS characteristics of the Ag/PMMA/ $(BzA)_2CuBr_4$ /Pt device are shown in Figure 11a, demonstrating the presence of bipolar RS behavior. An electroforming process occurs at approximately +0.5 V, with a CC of 10^{-3} A (Figure 11b). This process reveals that the ON switching happens at a SET voltage of approximately +0.2 V, while the OFF switching occurs at a RESET voltage of around -0.3 V (Figure 11c). Furthermore, an ON/OFF ratio is 10^8 . To examine reproducibility, the $I-V$ curves were measured using 10 distinct devices. Figure 11d demonstrates the high level of reproducibility in RS. The statistical analysis was conducted using the data from Figure 11e, where the mean values for HRS and LRS were calculated to be 1.1×10^{11} and $2.2 \times 10^2 \Omega$. The dots in Figure 11e correspond to the resistance values acquired from 10 individual devices. The endurance is evaluated for up to 2000 cycles in Figure 11f. The switching cycles maintained an ON/OFF ratio of 10^8 throughout the testing period. The switching cycles were controlled mainly by maintaining a resistance of $10^{10} \Omega$ for the HRS and $10^2 \Omega$ for the LRS. However, there was a slight variance in the HRS, which may be attributed to numerous or partially ruptured filaments. Retention time is measured in Figure 11g. HRS and LRS were maintained for 1000 s without causing fluctuation in the ON/OFF ratio of 10^8 .

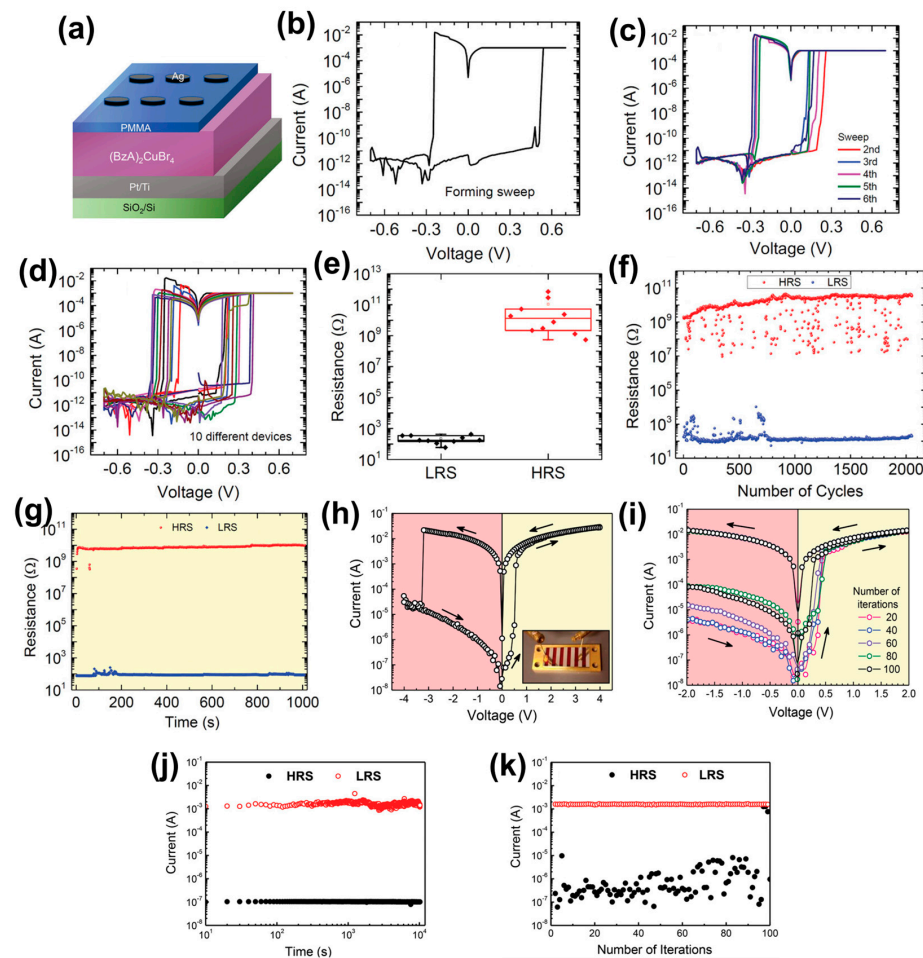


Figure 11. (a) Schematic of Ag/PMMA/ $(BzA)_2CuBr_4$ /Pt/Ti/SiO₂/Si device structure. (b) First voltage sweep of $(BzA)_2CuBr_4$ -based device. (c) Next five cycles of $(BzA)_2CuBr_4$ -based device. (d) Ten

different (BzA)₂CuBr₄-based devices. (e) Statistical resistance distribution of HRS and LRS. (f) Endurance of (BzA)₂CuBr₄-based device. (g) Retention time of (BzA)₂CuBr₄-based device. Reproduced with permission [96]. Copyright 2020, Wiley-VCH. (h) The typical *I*–*V* curves of ITO/Cs₃Sb₂I₉/Al devices. (i) The *I*–*V* curves measured. (j) Retention times of LRS and HRS. (k) Endurance of ITO/Cs₃Sb₂I₉/Al devices. Reproduced with permission [97]. Copyright 2021, Wiley-VCH.

Also, Paramanik et al. have demonstrated the performance of an RS memory device based on the Cs₃Sb₂I₉ perovskite as a switching layer [97]. The switching properties of the ITO/Cs₃Sb₂I₉/Al memory device were characterized. In Figure 11h, *I*–*V* curves are measured. Initially, the device had a value of 10^{−7} A. Such *I*–*V* curves imply that the Cs₃Sb₂I₉ perovskite-based memory device has a bipolar switching mode. The ON/OFF ratio of the Cs₃Sb₂I₉ device was 10⁴. As shown in Figure 11i, such a sequence of LRS and HRS in the Cs₃Sb₂I₉-based memory device could be repeated for 100 cycles, with the ON/OFF ratio around 10⁴.

Since the data retention property is essential for memory devices, the reliability was also measured with $-0.2 V_{\text{read}}$, as shown in Figure 11j. No significant fluctuation was observed within 10,000 s, inferring a reliable memory behavior in the devices. The endurance of RS in the Cs₃Sb₂I₉ devices was measured as shown in Figure 11k, and the resistance values were collected for up to 100 cycles. The devices switched between two distinct conducting states with a uniform RS behavior and without significant deterioration.

5. Conclusions and Perspectives

Three-dimensional HPs have rapidly advanced in different application areas, generating industry interest. The material exhibits hysteresis in its *I*–*V* relationship, caused by the generation and migration of defects in RS memory devices [98–100]. The field of HP-based RS memory devices is relatively new and offers a substantial opportunity for downstream research and exploratory studies. To develop robust RS memory devices, it is essential to have the capability to regulate the migration of ions [101]. Nevertheless, 3D HPs are prone to degradation due to moisture and the surrounding environment, rendering their devices more susceptible to deterioration. This review covered three main topics: an examination of the characteristics of 2D/quasi-2D HPs in comparison to 3D HPs, an explanation of the principles behind RS memory devices, and a discussion of recent advancements in the development of RS memory devices utilizing 2D/quasi-2D HPs. Several key research findings are summarized in Table 1. Regarding the requirements for future nonvolatile memory devices, 2D/quasi-2D HP-based RS memory devices should possess an ON/OFF ratio of greater than 10¹⁰, an endurance larger than 10³, and a retention duration exceeding 10 years. Recent research has shown that only the ON/OFF ratio of 2D/quasi-2D HP-based RS memory devices can almost match the specified criteria. Enhancing the endurance and retention characteristics still requires significant work. To make progress, it is essential to address significant obstacles. Also, to achieve this goal, research on various halide perovskites should be conducted. For example, chiral perovskites incorporating chiral organic ligands have also recently received much attention [102–104]. This review will inspire researchers to explore new avenues for advancing RS memory systems by utilizing 2D/quasi-2D HPs as innovative materials.

Table 1. Comparison of halide perovskite-based resistive switching memory devices.

Device Structure	ON/OFF Ratio	Endurance (Cycles)	Retention (s)
Ag/PMMA/HAPbI ₄ /ITO	10 ³	120	10 ⁴
Al/BAI(2D)/MAPbI _{3−x} Cl _x (3D)/ITO	10 ³	300	10 ⁴
Ag/PEA ₂ PbI ₄ /MAPbI ₃ /Pt	10 ⁷	2700	10 ⁴
Al/MAPbI _{3−x} Cl _x /MA ₂ PbI ₂ (SCN) ₂ /ITO	10 ⁴	1000	10 ⁴

Table 1. Cont.

Device Structure	ON/OFF Ratio	Endurance (Cycles)	Retention (s)
Ag/BA ₂ PbI ₄ /Pt	10 ⁷	250	10 ³
Ag/(PEA) ₂ Cs ₃ Pb ₄ I ₁₃ /Pt	10 ⁹	230	2 × 10 ³
Ag/PMMA/(BzA) ₂ CuBr ₄ /Pt	10 ⁸	2000	10 ³
ITO/Cs ₃ Sb ₂ I ₉ /Al	10 ⁴	100	10 ⁴

Author Contributions: Writing—original draft preparation, H.K. and M.H.; writing—review and editing, D.H. and Z.C.; supervision, C.W.M. All authors have read and agreed to the published version of the manuscript.

Funding: This research was supported by “Regional Innovation Strategy (RIS)” through the National Research Foundation of Korea (NRF), funded by the Ministry of Education (MOE) (2021RIS-004).

Data Availability Statement: No new data were created or analyzed in this study. Data sharing is not applicable to this article.

Conflicts of Interest: The authors declare no conflicts of interest.

References

- Kim, H.; Veerappan, G.; Park, J.H. Conducting Polymer Coated Non-Woven Graphite Fiber Film for Dye-Sensitized Solar Cells: Superior Pt- and FTO-Free Counter Electrodes. *Electrochim. Acta* **2014**, *137*, 164–168. [CrossRef]
- Wang, L.; Huang, L.; Tan, W.C.; Feng, X.; Chen, L.; Huang, X.; Ang, K.W. 2D Photovoltaic Devices: Progress and Prospects. *Small Methods* **2018**, *2*, 1700294. [CrossRef]
- Kim, H.; Kang, B.K.; Moon, C.W. Refractive Index Modulation for Metal Electrodeposition-Based Active Smart Window Applications. *Micromachines* **2024**, *15*, 334. [CrossRef]
- Kim, H.; Veerappan, G.; Wang, D.H.; Park, J.H. Large Area Platinum and Fluorine-Doped Tin Oxide-Free Dye Sensitized Solar Cells with Silver-Nanoplate Embedded Poly(3,4-Ethylenedioxythiophene) Counter Electrode. *Electrochim. Acta* **2016**, *187*, 218–223. [CrossRef]
- Chang, D.W.; Choi, H.J.; Filer, A.; Baek, J.B. Graphene in Photovoltaic Applications: Organic Photovoltaic Cells (OPVs) and Dye-Sensitized Solar Cells (DSSCs). *J. Mater. Chem. A Mater.* **2014**, *2*, 12136–12149. [CrossRef]
- Roslan, N.; Ya’acob, M.E.; Radzi, M.A.M.; Hashimoto, Y.; Jamaludin, D.; Chen, G. Dye Sensitized Solar Cell (DSSC) Greenhouse Shading: New Insights for Solar Radiation Manipulation. *Renew. Sustain. Energy Rev.* **2018**, *92*, 171–186. [CrossRef]
- Kim, H.; Han, J.S.; Choi, J.; Kim, S.Y.; Jang, H.W. Halide Perovskites for Applications beyond Photovoltaics. *Small Methods* **2018**, *2*, 1700310. [CrossRef]
- Qian, J.; Xu, B.; Tian, W. A Comprehensive Theoretical Study of Halide Perovskites ABX₃. *Org. Electron.* **2016**, *37*, 61–73. [CrossRef]
- Lang, L.; Yang, J.H.; Liu, H.R.; Xiang, H.J.; Gong, X.G. First-Principles Study on the Electronic and Optical Properties of Cubic ABX₃ Halide Perovskites. *Phys. Lett. A* **2014**, *378*, 290–293. [CrossRef]
- Murad, K.; Noman, M.; Khan, S.; Neffati, R.; Ashraf, M.W.; Murtaza, G. To Study the Structural, Electronic and Optical Properties of Predicted Stable Halide Perovskites ABX₃. *Phys. Scr.* **2023**, *98*, 075945. [CrossRef]
- Ben Sadok, R.; Plugaru, N.; Birsan, A.; Kuncser, V.; Hammoutène, D. Effect of Chemical Nature of Atoms on the Electronic, Dielectric, and Dynamical Properties of ABX₃ Halide Perovskite. *Int. J. Quantum Chem.* **2020**, *120*, e26172. [CrossRef]
- Akkerman, Q.A.; Manna, L. What Defines a Halide Perovskite? *ACS Energy Lett.* **2020**, *5*, 604–610. [CrossRef]
- Johnston, M.B.; Herz, L.M. Hybrid Perovskites for Photovoltaics: Charge-Carrier Recombination, Diffusion, and Radiative Efficiencies. *Acc. Chem. Res.* **2016**, *49*, 146–154. [CrossRef] [PubMed]
- Ma, L.; Hao, F.; Stoumpos, C.C.; Phelan, B.T.; Wasielewski, M.R.; Kanatzidis, M.G. Carrier Diffusion Lengths of over 500 nm in Lead-Free Perovskite CH₃NH₃SnI₃ Films. *J. Am. Chem. Soc.* **2016**, *138*, 14750–14755. [CrossRef] [PubMed]
- Van Le, Q.; Jang, H.W.; Kim, S.Y. Recent Advances toward High-Efficiency Halide Perovskite Light-Emitting Diodes: Review and Perspective. *Small Methods* **2018**, *2*, 1700419. [CrossRef]
- Lin, Y.H.; Pattanasattayavong, P.; Anthopoulos, T.D. Metal-Halide Perovskite Transistors for Printed Electronics: Challenges and Opportunities. *Adv. Mater.* **2017**, *29*, 1702838. [CrossRef] [PubMed]
- He, S.; Yu, X.; Wang, J.; Zhong, W.K.; Cheng, B.; Zhao, J. Attaining Inhibition of Sneak Current and Versatile Logic Operations in a Singular Halide Perovskite Memristive Device by Introducing Appropriate Interface Barriers. *Nanoscale* **2023**, *16*, 1102–1114. [CrossRef]
- Zhou, F.; Li, Z.; Lan, W.; Wang, Q.; Ding, L.; Jin, Z. Halide Perovskite, a Potential Scintillator for X-Ray Detection. *Small Methods* **2020**, *4*, 2000506. [CrossRef]

19. Han, B.; Zhao, J.; Luo, Z.; Cai, F.; Yuan, Z.; Zeng, H. Energy Storage Research of Metal Halide Perovskites for Rechargeable Batteries. *Nano Energy* **2023**, *115*, 108646. [[CrossRef](#)]
20. Kim, H.; Huynh, K.A.; Kim, S.Y.; Van Le, Q.; Jang, H.W. 2D and Quasi-2D Halide Perovskites: Applications and Progress. *Phys. Status Solidi Rapid Res. Lett.* **2020**, *14*, 1900435. [[CrossRef](#)]
21. Park, J.Y.; Lee, Y.H.; Kim, H.; Dou, L. Two-Dimensional Perovskite Heterostructures for Single Crystal Semiconductor Devices. *J. Appl. Phys.* **2023**, *134*, 060901. [[CrossRef](#)]
22. Kim, H.; Han, J.S.; Kim, S.G.; Kim, S.Y.; Jang, H.W. Halide Perovskites for Resistive Random-Access Memories. *J. Mater. Chem. C* **2019**, *7*, 5226–5234. [[CrossRef](#)]
23. Tyagi, P.; Arveson, S.M.; Tisdale, W.A. Colloidal Organohalide Perovskite Nanoplatelets Exhibiting Quantum Confinement. *J. Phys. Chem. Lett.* **2015**, *6*, 1911–1916. [[CrossRef](#)] [[PubMed](#)]
24. Ha, S.T.; Liu, X.; Zhang, Q.; Giovanni, D.; Sum, T.C.; Xiong, Q. Synthesis of Organic-Inorganic Lead Halide Perovskite Nanoplatelets: Towards High-Performance Perovskite Solar Cells and Optoelectronic Devices. *Adv. Opt. Mater.* **2014**, *2*, 838–844. [[CrossRef](#)]
25. Xu, X.; Pan, Y.; Zhong, Y.; Ran, R.; Shao, Z. Ruddlesden-Popper Perovskites in Electrocatalysis. *Mater. Horiz.* **2020**, *7*, 2519–2565. [[CrossRef](#)]
26. Yu, Y.; Zhang, D.; Yang, P. Ruddlesden-Popper Phase in Two-Dimensional Inorganic Halide Perovskites: A Plausible Model and the Supporting Observations. *Nano Lett.* **2017**, *17*, 5489–5494. [[CrossRef](#)]
27. Gong, J.; Hao, M.; Zhang, Y.; Liu, M.; Zhou, Y. Layered 2D Halide Perovskites beyond the Ruddlesden-Popper Phase: Tailored Interlayer Chemistries for High-Performance Solar Cells. *Angew. Chem. Int. Ed.* **2022**, *61*, e202112022. [[CrossRef](#)]
28. Li, F.; Xie, Y.; Hu, Y.; Long, M.; Zhang, Y.; Xu, J.; Qin, M.; Lu, X.; Liu, M. Effects of Alkyl Chain Length on Crystal Growth and Oxidation Process of Two-Dimensional Tin Halide Perovskites. *ACS Energy Lett.* **2020**, *5*, 1422–1429. [[CrossRef](#)]
29. González-Carrero, S.; Galian, R.E.; Pérez-Prieto, J. Organometal Halide Perovskites: Bulk Low-Dimension Materials and Nanoparticles. *Part. Part. Syst. Charact.* **2015**, *32*, 709–720. [[CrossRef](#)]
30. Cinquino, M.; Fieramosca, A.; Mastria, R.; Polimeno, L.; Moliterni, A.; Olieric, V.; Matsugaki, N.; Panico, R.; De Giorgi, M.; Gigli, G.; et al. Managing Growth and Dimensionality of Quasi 2D Perovskite Single-Crystalline Flakes for Tunable Excitons Orientation. *Adv. Mater.* **2021**, *33*, 2102326. [[CrossRef](#)]
31. Singldinger, A.; Gramlich, M.; Gruber, C.; Lampe, C.; Urban, A.S. Nonradiative Energy Transfer between Thickness-Controlled Halide Perovskite Nanoplatelets. *ACS Energy Lett.* **2020**, *5*, 1380–1385. [[CrossRef](#)] [[PubMed](#)]
32. Liu, N.; Luo, J.; Guo, Q.; Du, P.; Gao, L.; Niu, G.; Song, B.; Tang, J. Reduced Self-Absorption of Quasi-2D Perovskites and Their Application in Color Conversion Layers. *Adv. Opt. Mater.* **2023**, *11*, 2202118. [[CrossRef](#)]
33. Deng, S.; Shi, E.; Yuan, L.; Jin, L.; Dou, L.; Huang, L. Long-Range Exciton Transport and Slow Annihilation in Two-Dimensional Hybrid Perovskites. *Nat. Commun.* **2020**, *11*, 664. [[CrossRef](#)] [[PubMed](#)]
34. Wang, K.; Wu, C.; Yang, D.; Jiang, Y.; Priya, S. Quasi-Two-Dimensional Halide Perovskite Single Crystal Photodetector. *ACS Nano* **2018**, *12*, 4919–4929. [[CrossRef](#)] [[PubMed](#)]
35. Akriti; Shi, E.; Shiring, S.B.; Yang, J.; Atencio-Martinez, C.L.; Yuan, B.; Hu, X.; Gao, Y.; Finkenauer, B.P.; Pistone, A.J.; et al. Layer-by-Layer Anionic Diffusion in Two-Dimensional Halide Perovskite Vertical Heterostructures. *Nat. Nanotechnol.* **2021**, *16*, 584–591. [[CrossRef](#)]
36. Etgar, L. The Merit of Perovskite's Dimensionality; Can This Replace the 3D Halide Perovskite? *Energy Environ. Sci.* **2018**, *11*, 234–242. [[CrossRef](#)]
37. Blancon, J.C.; Stier, A.V.; Tsai, H.; Nie, W.; Stoumpos, C.C.; Traoré, B.; Pedesseau, L.; Kepenekian, M.; Katsutani, F.; Noe, G.T.; et al. Scaling Law for Excitons in 2D Perovskite Quantum Wells. *Nat. Commun.* **2018**, *9*, 2254. [[CrossRef](#)]
38. Zalamai, V.V.; Syrbu, N.N.; Stamov, I.G.; Beril, S.I. Wannier-Mott Excitons in GaSe Single Crystals. *J. Opt.* **2020**, *22*, 085402. [[CrossRef](#)]
39. Agranovich, V.M.; Basko, D.M.; Schmidt, K.; LaRocca, G.C.; Bassani, F.; Forrest, S.; Leo, K.; Lidzey, D. Charged Frenkel Excitons in Organic Crystals. *Chem. Phys.* **2001**, *272*, 159–169. [[CrossRef](#)]
40. Smith, I.C.; Hoke, E.T.; Solis-Ibarra, D.; McGehee, M.D.; Karunadasa, H.I. A Layered Hybrid Perovskite Solar-Cell Absorber with Enhanced Moisture Stability. *Angew. Chem. Int. Ed.* **2014**, *53*, 11232–11235. [[CrossRef](#)]
41. Han, J.S.; Van Le, Q.; Choi, J.; Hong, K.; Moon, C.W.; Kim, T.L.; Kim, H.; Kim, S.Y.; Jang, H.W. Air-Stable Cesium Lead Iodide Perovskite for Ultra-Low Operating Voltage Resistive Switching. *Adv. Funct. Mater.* **2018**, *28*, 1705783. [[CrossRef](#)]
42. Ge, J.; Chaker, M. Oxygen Vacancies Control Transition of Resistive Switching Mode in Single-Crystal TiO₂ Memory Device. *ACS Appl. Mater. Interfaces* **2017**, *9*, 16327–16334. [[CrossRef](#)] [[PubMed](#)]
43. Choi, J.; Park, S.; Lee, J.; Hong, K.; Kim, D.H.; Moon, C.W.; Park, G.D.; Suh, J.; Hwang, J.; Kim, S.Y.; et al. Organolead Halide Perovskites for Low Operating Voltage Multilevel Resistive Switching. *Adv. Mater.* **2016**, *28*, 6562–6567. [[CrossRef](#)] [[PubMed](#)]
44. Schönhals, A.; Rosário, C.M.M.; Hoffmann-Eifert, S.; Waser, R.; Menzel, S.; Wouters, D.J. Role of the Electrode Material on the RESET Limitation in Oxide ReRAM Devices. *Adv. Electron. Mater.* **2018**, *4*, 1700243. [[CrossRef](#)]
45. Kwak, K.J.; Lee, D.E.; Kim, S.J.; Jang, H.W. Halide Perovskites for Memristive Data Storage and Artificial Synapses. *J. Phys. Chem. Lett.* **2021**, *12*, 8999–9010. [[CrossRef](#)] [[PubMed](#)]
46. Di, J.; Du, J.; Lin, Z.; Liu, S.; Ouyang, J.; Chang, J. Recent Advances in Resistive Random Access Memory Based on Lead Halide Perovskite. *InfoMat* **2021**, *3*, 293–315. [[CrossRef](#)]

47. Jeong, D.N.; Yang, J.M.; Park, N.G. Roadmap on Halide Perovskite and Related Devices. *Nanotechnology* **2020**, *31*, 152001. [[CrossRef](#)]
48. Choi, J.; Han, J.S.; Hong, K.; Kim, S.Y.; Jang, H.W. Organic-Inorganic Hybrid Halide Perovskites for Memories, Transistors, and Artificial Synapses. *Adv. Mater.* **2018**, *30*, e1704002. [[CrossRef](#)]
49. Prakash, A.; Jana, D.; Maikap, S. TaOx-Based Resistive Switching Memories: Prospective and Challenges. *Nanoscale Res. Lett.* **2013**, *8*, 1–17. [[CrossRef](#)]
50. Thien, G.S.H.; Sarjidan, M.A.M.; Talik, N.A.; Goh, B.T.; Yap, B.K.; He, Z.; Chan, K.Y. Electrode Dependence in Halide Perovskite Memories: Resistive Switching Behaviours. *Mater. Chem. Front.* **2022**, *6*, 3125–3142. [[CrossRef](#)]
51. Satapathi, S.; Raj, K.; Yukta; Afroz, M.A. Halide-Perovskite-Based Memristor Devices and Their Application in Neuromorphic Computing. *Phys. Rev. Appl.* **2022**, *18*, 017001. [[CrossRef](#)]
52. How, G.T.S.; Talik, N.A.; Yap, B.K.; Nakajima, H.; Tunmee, S.; Goh, B.T. Multiple Resistive Switching Behaviours of CH₃NH₃PbI₃ Perovskite Film with Different Metal Electrodes. *Appl. Surf. Sci.* **2019**, *473*, 194–202. [[CrossRef](#)]
53. Nowak, E.; Chłopocka, E.; Szybowicz, M. ZnO and ZnO-Based Materials as Active Layer in Resistive Random-Access Memory (RRAM). *Crystals* **2023**, *13*, 416. [[CrossRef](#)]
54. Poddar, S.; Zhang, Y.; Chen, Z.; Ma, Z.; Fu, Y.; Ding, Y.; Chan, C.L.J.; Zhang, Q.; Zhang, D.; Song, Z.; et al. Image Processing with a Multi-Level Ultra-Fast Three Dimensionally Integrated Perovskite Nanowire Array. *Nanoscale Horiz.* **2022**, *7*, 759–769. [[CrossRef](#)]
55. Wu, M.C.; Ting, Y.H.; Chen, J.Y.; Wu, W.W. Low Power Consumption Nanofilamentary ECM and VCM Cells in a Single Sidewall of High-Density VRRAM Arrays. *Adv. Sci.* **2019**, *6*, 1902363. [[CrossRef](#)] [[PubMed](#)]
56. Michieletti, F.; Chen, S.; Weber, C.; Ricciardi, C.; Ohno, T.; Valov, I. Influence of Active Electrode Impurity on Memristive Characteristics of ECM Devices. *J. Solid State Electrochem.* **2024**, *28*, 1735–1741. [[CrossRef](#)]
57. Von Witzleben, M.; Hennen, T.; Kindsmüller, A.; Menzel, S.; Waser, R.; Böttger, U. Study of the SET Switching Event of VCM-Based Memories on a Picosecond Timescale. *J. Appl. Phys.* **2020**, *127*, 204501. [[CrossRef](#)]
58. Ahn, J.; Bang, J.; Kim, Y.M.; Oh, S.; Kim, S.Y.; Sung, Y.M.; Oh, S.J. Designing Metal Halide Perovskite Nanoparticle-Based Resistive Random-Access Memory Devices through Chemical Treatments. *Mater. Today Nano* **2023**, *24*, 100388. [[CrossRef](#)]
59. Lübben, M.; Valov, I. Active Electrode Redox Reactions and Device Behavior in ECM Type Resistive Switching Memories. *Adv. Electron. Mater.* **2019**, *5*, 1800933. [[CrossRef](#)]
60. Lv, H.; Xu, X.; Liu, H.; Liu, R.; Liu, Q.; Banerjee, W.; Sun, H.; Long, S.; Li, L.; Liu, M. Evolution of Conductive Filament and Its Impact on Reliability Issues in Oxide-Electrolyte Based Resistive Random Access Memory. *Sci. Rep.* **2015**, *5*, 7764. [[CrossRef](#)]
61. Kim, S.G.; Van Le, Q.; Han, J.S.; Kim, H.; Choi, M.J.; Lee, S.A.; Kim, T.L.; Kim, S.B.; Kim, S.Y.; Jang, H.W. Dual-Phase All-Inorganic Cesium Halide Perovskites for Conducting-Bridge Memory-Based Artificial Synapses. *Adv. Funct. Mater.* **2019**, *29*, 1906686. [[CrossRef](#)]
62. Waser, R.; Menzel, S.; Rana, V. Recent Progress in Redox-Based Resistive Switching. In Proceedings of the 2012 IEEE International Symposium on Circuits and Systems, Seoul, Republic of Korea, 20–23 May 2012; pp. 1596–1599.
63. Cuhadar, C.; Kim, S.-G.; Yang, J.-M.; Seo, J.-Y.; Lee, D.; Park, N.-G. All-Inorganic Bismuth Halide Perovskite-Like Materials A₃Bi₂I₉ and A₃Bi_{1.8}Na_{0.2}I_{8.6} (A = Rb and Cs) for Low-Voltage Switching Resistive Memory. *ACS Appl. Mater. Interfaces* **2018**, *10*, 29741–29749. [[CrossRef](#)] [[PubMed](#)]
64. Valov, I. Interfacial Interactions and Their Impact on Redox-Based Resistive Switching Memories (ReRAMs). *Semicond. Sci. Technol.* **2017**, *32*, 093006. [[CrossRef](#)]
65. Kim, W.; Wouters, D.J.; Menzel, S.; Rodenbacher, C.; Waser, R.; Rana, V. Lowering Forming Voltage and Forming-Free Behavior of Ta₂O₅ ReRAM Devices. In Proceedings of the 2016 46th European Solid-State Device Research Conference (ESSDERC), Lausanne, Switzerland, 12–15 September 2016; pp. 164–167.
66. Praveen, P.; Rose, T.P.; Saji, K.J. Top Electrode Dependent Resistive Switching in M/ZnO/ITO Memristors, M = Al, ITO, Cu, and Au. *Microelectron. J.* **2022**, *121*, 105388. [[CrossRef](#)]
67. Fra, V.; Shahrabi, E.; Leblebici, Y.; Ricciardi, C. Investigation on the Stabilizing Effect of Titanium in HfO₂-Based Resistive Switching Devices with Tungsten Electrode. *Front. Nanotechnol.* **2020**, *2*, 592684. [[CrossRef](#)]
68. Valov, I.; Waser, R. Comment on Real-Time Observation on Dynamic Growth/Dissolution of Conductive Filaments in Oxide-Electrolyte-Based ReRAM. *Adv. Mater.* **2013**, *25*, 162–164. [[CrossRef](#)]
69. Kim, S.G.; Han, J.S.; Kim, H.; Kim, S.Y.; Jang, H.W. Recent Advances in Memristive Materials for Artificial Synapses. *Adv. Mater. Technol.* **2018**, *3*, 1800457. [[CrossRef](#)]
70. Han, J.S.; Van Le, Q.; Choi, J.; Kim, H.; Kim, S.G.; Hong, K.; Moon, C.W.; Kim, T.L.; Kim, S.Y.; Jang, H.W. Lead-Free All-Inorganic Cesium Tin Iodide Perovskite for Filamentary and Interface-Type Resistive Switching toward Environment-Friendly and Temperature-Tolerant Nonvolatile Memories. *ACS Appl. Mater. Interfaces* **2019**, *11*, 8155–8163. [[CrossRef](#)]
71. Han, J.S.; Van Le, Q.; Kim, H.; Lee, Y.J.; Lee, D.E.; Im, I.H.; Lee, M.K.; Kim, S.J.; Kim, J.; Kwak, K.J.; et al. Lead-Free Dual-Phase Halide Perovskites for Preconditioned Conducting-Bridge Memory. *Small* **2020**, *16*, 2003225. [[CrossRef](#)]
72. Chauhan, M.; Singh, R.; Sharma, S.K. Electro-Optically Tunable Passivated Double-Cation Perovskite-Based ReRAM for Low-Power Memory Applications. *ACS Appl. Electron. Mater.* **2024**, *6*, 2709–2719. [[CrossRef](#)]
73. Zhou, C.; Tarasov, A.B.; Goodilin, E.A.; Chen, P.; Wang, H.; Chen, Q. Recent Strategies to Improve Moisture Stability in Metal Halide Perovskites Materials and Devices. *J. Energy Chem.* **2022**, *65*, 219–235. [[CrossRef](#)]

74. DI, J.; Lin, Z.; Su, J.; Wang, J.; Zhang, J.; Liu, S.; Chang, J.; Hao, Y. Two-Dimensional $(C_6H_5C_2H_4NH_3)_2PbI_4$ Perovskite Single Crystal Resistive Switching Memory Devices. *IEEE Electron. Device Lett.* **2021**, *42*, 327–330. [[CrossRef](#)]
75. Liu, B.; Lai, J.; Wu, D.; Li, L.; Kang, K.; Hu, W.; Tang, X. High-Performance Resistive Random Access Memories Based on Two-Dimensional $HAPbI_4$ Organic-Inorganic Hybrid Perovskite. *J. Phys. Chem. Lett.* **2022**, *13*, 7653–7659. [[CrossRef](#)] [[PubMed](#)]
76. Xia, F.; Xu, Y.; Li, B.; Hui, W.; Zhang, S.; Zhu, L.; Xia, Y.; Chen, Y.; Huang, W. Improved Performance of $CH_3NH_3PbI_{3-x}Cl_x$ Resistive Switching Memory by Assembling 2D/3D Perovskite Heterostructures. *ACS Appl. Mater. Interfaces* **2020**, *12*, 1543–15445. [[CrossRef](#)] [[PubMed](#)]
77. Lee, S.M.; Kim, H.; Kim, D.H.; Kim, W.B.; Lee, J.M.; Choi, J.; Shin, H.; Han, G.S.; Jang, H.W.; Jung, H.S. Tailored 2D/3D Halide Perovskite Heterointerface for Substantially Enhanced Endurance in Conducting Bridge Resistive Switching Memory. *ACS Appl. Mater. Interfaces* **2020**, *12*, 17039–17045. [[CrossRef](#)]
78. Kim, H.S.; Lee, C.R.; Im, J.H.; Lee, K.B.; Moehl, T.; Marchioro, A.; Moon, S.J.; Humphry-Baker, R.; Yum, J.H.; Moser, J.E.; et al. Lead Iodide Perovskite Sensitized All-Solid-State Submicron Thin Film Mesoscopic Solar Cell with Efficiency Exceeding 9%. *Sci. Rep.* **2012**, *2*, 591. [[CrossRef](#)]
79. Burschka, J.; Pellet, N.; Moon, S.J.; Humphry-Baker, R.; Gao, P.; Nazeeruddin, M.K.; Grätzel, M. Sequential Deposition as a Route to High-Performance Perovskite-Sensitized Solar Cells. *Nature* **2013**, *499*, 316–319. [[CrossRef](#)]
80. Jeon, N.J.; Noh, J.H.; Kim, Y.C.; Yang, W.S.; Ryu, S.; Seok, S. II Solvent Engineering for High-Performance Inorganic-Organic Hybrid Perovskite Solar Cells. *Nat. Mater.* **2014**, *13*, 897–903. [[CrossRef](#)]
81. Bai, Y.; Xiao, S.; Hu, C.; Zhang, T.; Meng, X.; Lin, H.; Yang, Y.; Yang, S. Dimensional Engineering of a Graded 3D-2D Halide Perovskite Interface Enables Ultrahigh Voc Enhanced Stability in the p-i-n Photovoltaics. *Adv. Energy Mater.* **2017**, *7*, 1701038. [[CrossRef](#)]
82. Li, M.H.; Yeh, H.H.; Chiang, Y.H.; Jeng, U.S.; Su, C.J.; Shiu, H.W.; Hsu, Y.J.; Kosugi, N.; Ohigashi, T.; Chen, Y.A.; et al. Highly Efficient 2D/3D Hybrid Perovskite Solar Cells via Low-Pressure Vapor-Assisted Solution Process. *Adv. Mater.* **2018**, *30*, e1801401. [[CrossRef](#)]
83. Chen, P.; Bai, Y.; Wang, S.; Lyu, M.; Yun, J.H.; Wang, L. In Situ Growth of 2D Perovskite Capping Layer for Stable and Efficient Perovskite Solar Cells. *Adv. Funct. Mater.* **2018**, *28*, 1706923. [[CrossRef](#)]
84. Pan, X.; Chen, X.; Duan, J.; Long, Y.; Wu, Y.; Tang, J.; Ma, G.; Zhang, J.; Wang, H. Three-Dimensional/Two-Dimensional Perovskite-Resistive Random-Access Memory with Low SET Voltage and High Stability. *ACS Appl. Electron. Mater.* **2023**, *5*, 6908–6917. [[CrossRef](#)]
85. Zhang, H.; Zhuang, J.; Liu, X.; Ma, Z.; Guo, H.; Zheng, R.; Zhao, S.; Zhang, F.; Xiao, Z.; Wang, H.; et al. Defect Passivation Strategy for Inorganic $CsPbI_2Br$ Perovskite Solar Cell with a High-Efficiency of 16.77%. *J. Mater. Sci. Technol.* **2021**, *82*, 40–46. [[CrossRef](#)]
86. Jeong, H.J.; Park, C.; Jeon, H.; Lee, K.N.; Lee, J.; Lim, S.C.; Namkoong, G.; Jeong, M.S. Quasi-2D Halide Perovskite Memory Device Formed by Acid-Base Binary Ligand Solution Composed of Oleylamine and Oleic Acid. *ACS Appl. Mater. Interfaces* **2021**, *13*, 40891–40900. [[CrossRef](#)] [[PubMed](#)]
87. Seo, J.-Y.; Choi, J.; Kim, H.-S.; Kim, J.; Yang, J.-M.; Cuhadar, C.; Han, J.S.; Kim, S.-J.; Lee, D.; Jang, H.W.; et al. Wafer-Scale Reliable Switching Memory Based on 2-Dimensional Layered Organic-Inorganic Halide Perovskite. *Nanoscale* **2017**, *9*, 15278–15285. [[CrossRef](#)]
88. Kim, K.M.; Jeong, D.S.; Hwang, C.S. Nanofilamentary Resistive Switching in Binary Oxide System; a Review on the Present Status and Outlook. *Nanotechnology* **2011**, *22*, 254002. [[CrossRef](#)]
89. Kim, H.; Choi, M.J.; Suh, J.M.; Han, J.S.; Kim, S.G.; Van Le, Q.; Kim, S.Y.; Jang, H.W. Quasi-2D Halide Perovskites for Resistive Switching Devices with ON/OFF Ratios above 10^9 . *NPG Asia Mater.* **2020**, *12*, 21. [[CrossRef](#)]
90. Ng, Y.F.; Kulkarni, S.A.; Parida, S.; Jamaludin, N.F.; Yantara, N.; Bruno, A.; Soci, C.; Mhaisalkar, S.; Mathews, N. Highly Efficient Cs-Based Perovskite Light-Emitting Diodes Enabled by Energy Funnelling. *Chem. Commun.* **2017**, *53*, 12004–12007. [[CrossRef](#)]
91. Gebhardt, J.; Kim, Y.; Rappe, A.M. Influence of the Dimensionality and Organic Cation on Crystal and Electronic Structure of Organometallic Halide Perovskites. *J. Phys. Chem. C* **2017**, *121*, 6569–6574. [[CrossRef](#)]
92. Ma, S.; Cai, M.; Cheng, T.; Ding, X.; Shi, X.; Alsaedi, A.; Hayat, T.; Ding, Y.; Tan, Z.; Dai, S. Two-Dimensional Organic-Inorganic Hybrid Perovskite: From Material Properties to Device Applications. *Sci. China Mater.* **2018**, *61*, 1257–1277. [[CrossRef](#)]
93. Park, J.; Biju, K.P.; Jung, S.; Lee, W.; Lee, J.; Kim, S.; Park, S.; Shin, J.; Hwang, H. Multibit Operation of TiO_x -Based ReRAM by Schottky Barrier Height Engineering. *IEEE Electron. Device Lett.* **2011**, *32*, 476–478. [[CrossRef](#)]
94. Chen, S.C.; Lou, J.C.; Chien, C.H.; Liu, P.T.; Chang, T.C. An Interfacial Investigation of High-Dielectric Constant Material Hafnium Oxide on Si Substrate. *Thin Solid Films* **2005**, *488*, 167–172. [[CrossRef](#)]
95. Kim, Y.; Baik, S.J.; Shin, H. Vertically Oriented 2D Layered Perovskite-Based Resistive Random Access Memory (ReRAM) Crossbar Arrays. *Curr. Appl. Phys.* **2022**, *44*, 46–54. [[CrossRef](#)]
96. Kim, S.Y.; Yang, J.M.; Choi, E.S.; Park, N.G. Layered $(C_6H_5CH_2NH_3)_2CuBr_4$ Perovskite for Multilevel Storage Resistive Switching Memory. *Adv. Funct. Mater.* **2020**, *30*, 2002653. [[CrossRef](#)]
97. Paramanik, S.; Maiti, A.; Chatterjee, S.; Pal, A.J. Large Resistive Switching and Artificial Synaptic Behaviors in Layered $Cs_3Sb_2I_9$ Lead-Free Perovskite Memory Devices. *Adv. Electron. Mater.* **2022**, *8*, 2100237. [[CrossRef](#)]
98. Berruet, M.; Pérez-Martínez, J.C.; Romero, B.; Gonzales, C.; Al-Mayouf, A.M.; Guerrero, A.; Bisquert, J. Physical Model for the Current–Voltage Hysteresis and Impedance of Halide Perovskite Memristors. *ACS Energy Lett.* **2022**, *7*, 1214–1222. [[CrossRef](#)]

99. Bisquert, J.; Bou, A.; Guerrero, A.; Hernández-Balaguera, E. Resistance Transient Dynamics in Switchable Perovskite Memristors. *APL Mach. Learn.* **2023**, *1*, 036101. [[CrossRef](#)]
100. Hernández-Balaguera, E.; Muñoz-Díaz, L.; Bou, A.; Romero, B.; Ilyassov, B.; Guerrero, A.; Bisquert, J. Long-Term Potentiation Mechanism of Biological Postsynaptic Activity in Neuro-Inspired Halide Perovskite Memristors. *Neuromorph. Comput. Eng.* **2023**, *3*, 024005. [[CrossRef](#)]
101. Sakhatskyi, K.; John, R.A.; Guerrero, A.; Tsarev, S.; Sabisch, S.; Das, T.; Matt, G.J.; Yakunin, S.; Cherniukh, I.; Kotyrba, M.; et al. Assessing the Drawbacks and Benefits of Ion Migration in Lead Halide Perovskites. *ACS Energy Lett.* **2022**, *7*, 3401–3414. [[CrossRef](#)]
102. Long, G.; Jiang, C.; Sabatini, R.; Yang, Z.; Wei, M.; Quan, L.N.; Liang, Q.; Rasmita, A.; Askerka, M.; Walters, G.; et al. Spin Control in Reduced-Dimensional Chiral Perovskites. *Nat. Photonics* **2018**, *12*, 528–533. [[CrossRef](#)]
103. Long, G.; Sabatini, R.; Saidaminov, M.I.; Lakhwani, G.; Rasmita, A.; Liu, X.; Sargent, E.H.; Gao, W. Chiral-Perovskite Optoelectronics. *Nat. Rev. Mater.* **2020**, *5*, 423–439. [[CrossRef](#)]
104. Niu, X.; Zeng, Z.; Wang, Z.; Lu, H.; Sun, B.; Zhang, H.-L.; Chen, Y.; Du, Y.; Long, G. The First Chiral Cerium Halide towards Circularly-Polarize Luminescence in the UV Region. *Sci. China Chem.* **2024**, *67*, 1961–1968. [[CrossRef](#)]

Disclaimer/Publisher’s Note: The statements, opinions and data contained in all publications are solely those of the individual author(s) and contributor(s) and not of MDPI and/or the editor(s). MDPI and/or the editor(s) disclaim responsibility for any injury to people or property resulting from any ideas, methods, instructions or products referred to in the content.